Computation of geostrophic streamfunction, its derivatives, and error estimates from an array of CPIES in Drake Passage

Y. L. Firing, Teresa K. Chereskin, D. R. Watts, K. L. Tracey, Christine Provost

Computation of Geostrophic Streamfunction, Its Derivatives, and Error Estimates from an Array of CPIES in Drake Passage

Y. L. FIRING* AND T. K. CHERESKIN

Scripps Institution of Oceanography, University of California, San Diego, La Jolla, California

D. R. WATTS AND K. L. TRACEY

Graduate School of Oceanography, University of Rhode Island, Narragansett, Rhode Island

C. PROVOST

LOCEAN, UMR 7159, Université Pierre et Marie Curie, CNRS, IRD, MNHN, Paris, France

(Manuscript received 11 July 2013, in final form 9 November 2013)

ABSTRACT

Current and pressure-recording inverted echo sounders (CPIES) were deployed in an eddy-resolving local dynamics array (LDA) in the eddy-rich polar frontal zone (PFZ) in Drake Passage as part of the cDrake experiment. Methods are described for calculating barotropic and baroclinic geostrophic streamfunction and its first, second, and third derivatives by objective mapping of current, pressure, or geopotential height anomaly data from a two-dimensional array of CPIES like the cDrake LDA.

Modifications to previous methods result in improved dimensional error estimates on velocity and higher streamfunction derivatives. Simulations are used to test the reproduction of higher derivatives of streamfunction and to verify mapping error estimates. Three-day low-pass-filtered velocity in and around the cDrake LDA can be mapped with errors of $0.04\,\mathrm{m\,s^{-1}}$ at 4000 dbar, increasing to $0.13\,\mathrm{m\,s^{-1}}$ at the sea surface; these errors are small compared to typical speeds observed at these levels, 0.2 and $0.65\,\mathrm{m\,s^{-1}}$, respectively. Errors on vorticity are $9 \times 10^{-6}\,\mathrm{s^{-1}}$ near the surface, decreasing with depth to $3 \times 10^{-6}\,\mathrm{s^{-1}}$ at 4000 dbar, whereas vorticities in the PFZ eddy field are $4 \times 10^{-5}\,\mathrm{s^{-1}}$ (surface) to $1.3 \times 10^{-5}\,\mathrm{s^{-1}}$ (4000 dbar). Vorticity gradient errors range from 4×10^{-10} to $2 \times 10^{-10}\,\mathrm{m^{-1}\,s^{-1}}$, just under half the size of typical PFZ vorticity gradients. Comparisons between cDrake mapped temperature and velocity fields and independent observations (moored current and temperature, lowered acoustic Doppler current profiler velocity, and satellite-derived surface currents) help validate the cDrake method and results.

1. Introduction

As part of the cDrake experiment, an array of 42 current- and pressure-recording inverted echo sounders (CPIES) was deployed across Drake Passage from November–December 2007 to November–December 2011 (Fig. 1; Chereskin et al. 2009, 2012). The 3×7 local dynamics array (LDA) in the polar frontal zone (PFZ) provides two-dimensional sampling and the potential to estimate time-varying velocity and vorticity in this eddy-rich area. An empirical lookup table for hydrographic property profiles indexed by acoustic travel time between the surface and a preselected reference depth, known as a gravest empirical mode (GEM) table (Meinen and Watts 2000; Watts et al. 2001b), was constructed from nearly 600 CTD and Argo profiles in the cDrake region (Cutting 2010) and provides the ability to convert travel time to hydrographic profiles. Here, we explain the method for computing geostrophic baroclinic streamfunction from the bottom-to-surface round-trip acoustic travel time and a GEM, and geostrophic barotropic streamfunction from bottom pressure and currents. For both streamfunctions, we describe the procedure for optimally estimating their derivatives in

* Current affiliation: California Institute of Technology, Pasadena, California.

Corresponding author address: Y. L. Firing, Jet Propulsion Laboratory, California Institute of Technology, 4800 Oak Grove Dr., M/S 233-305, Pasadena, CA 91109.
E-mail: yfiring@caltech.edu

DOI: 10.1175/JTECH-D-13-00142.1

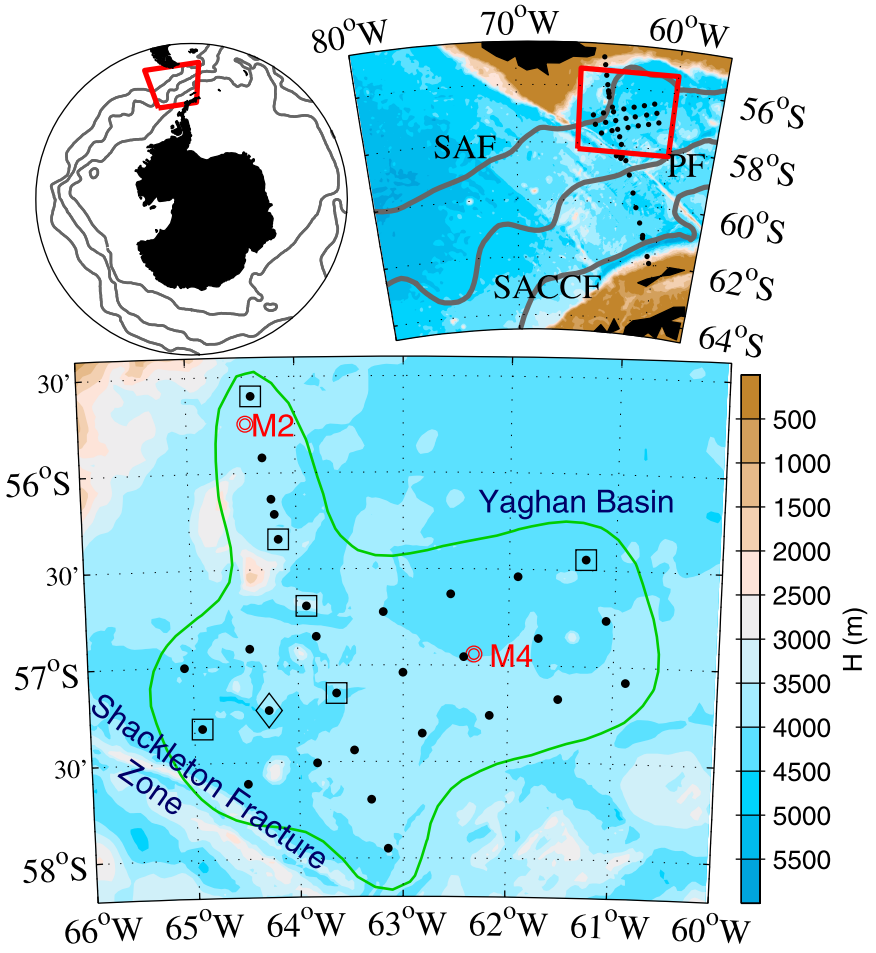

FIG. 1. (top left) Southern Ocean map with Orsi et al. (1995) fronts (gray lines), with box marking the region from which hydrographic profiles used in the cDrake GEMs (section 2, appendix A) were drawn. (top right) Enlargement of the boxed area showing cDrake CPIES sites over Orsi et al. (1995) fronts (gray lines) and bathymetry (described in text), with box outlining the LDA area, shown below. (Bottom) CPIES sites (dots) and bathymetry (filled contours) in the LDA, with M2 and M4 mooring sites (circles). Site B02 is indicated by a diamond and the six LDA tip-step sites (A02, C03, C05, C19, C07, G03) by squares. The baroclinic and deep reference fields were mapped within the 13% variance error contour (green) of the bottom reference ψ map (designated as the good mapping region, see section 5).

order to compute velocity, vorticity, and vorticity gradients in a two-dimensional array like the cDrake LDA.

Two-dimensional arrays of inverted echo sounders, together with current measurements, have been used to compute geostrophic streamfunction and velocity in several experiments, including studies in the Gulf Stream [Synoptic Ocean Prediction Experiment (SYNOP); Tracey et al. 1997; Watts et al. 2001a], Subantarctic Front [Subantarctic Flux and Dynamics Experiment (SAFDE); Meinen and Luther 2002; Tracey et al. 2006], and Kuroshio Extension System Study (KESS); Donohue et al. 2010]. Some of these studies have used objective mapping (Bretherton et al. 1976) with the assumption of nondivergence (Qian and Watts 1992; Watts et al. 2001a) to produce barotropic (bottom reference, depth independent) streamfunction and velocity from bottom pressure and velocity data, and baroclinic streamfunction and velocity (both referenced to zero at the bottom) from the inverted echo sounders (IES)-measured travel times in combination with a GEM. Optimal interpolation parameters (covariance length scale and noise) have been determined by fitting an a priori Gaussian covariance function for streamfunction to observed spatial correlations from the pressure-recording inverted echo sounders (PIES) data. Iterative mapping is used to capture variance at multiple time and space scales.

In previous studies (Meinen and Luther 2002; Donohue et al. 2010) baroclinic velocity has been computed by

mapping travel time data to travel time and the horizontal gradients of travel time and then converting them to velocity by using derivatives of geopotential anomaly with respect to travel time. These derivatives are estimated by finite differencing of a lookup table for geopotential anomaly as a function of travel time and pressure. Baroclinic velocity profiles computed by this method have been found to compare well with directly measured currents in SAFDE (Watts et al. 2001b). Several studies have shown that Southern Ocean density and temperature variance can be captured by a GEM (Sun and Watts 2001; Swart et al. 2010; Meijers et al. 2011a,b; Behnisch et al. 2013), making GEM-based prediction of baroclinic velocity profiles in the cDrake area a promising prospect. Howden and Watts (1999) objectively mapped spatial derivatives of velocity in the Gulf Stream by applying a linear operator to the correlation functions (Bretherton et al. 1976).

In previous experiments where objective mapping was used to compute streamfunction and velocity from an array of CPIES (e.g., Tracey et al. 1997; Meinen and Luther 2002; Donohue et al. 2010), the array has been centered under the jet. The cDrake LDA, in contrast, was located in the high-variability PFZ, between the mean positions of the two main Antarctic Circumpolar Current (ACC) jets (the Subantarctic Front to the north and Polar Front to the south). A main focus of this work is on resolving the strong mesoscale variability in the PFZ and making accurate estimates of uncertainty in a nonlinear regime, which requires attention to higher-order terms. We build on previous work to extend the objective mapping procedure to third derivatives of geostrophic streamfunction, with variable Coriolis parameter f (appendix B). We also explain the advantages of converting travel time τ to geopotential Φ for time series at each observation site (using the GEM lookup tables, described in appendix A), and mapping directly to velocities and their derivatives without finite differencing.

The principal objectives of this paper are 1) to describe methods for the estimation of dynamical variables and their uncertainties from a two-dimensional array of CPIES using objective mapping, and 2) to verify the mapped variables and uncertainty estimates against independent measurements of velocity and temperature, and simulated vorticity and vorticity gradient fields. The datasets are described in section 2. The objective mapping process as implemented for the cDrake LDA, including error estimation and selection of mapping parameters based on the observations, is explained in section 3. In section 4, simulated analytic fields are used to test the mapping and error estimation procedure for geostrophic streamfunction and its derivatives, including vorticity and vorticity gradients. Section 5 gives an overview of the cDrake mapped geostrophic velocity, vorticity, and vorticity gradient fields and the corresponding error maps. Comparisons with synoptic velocity profiles, moored current and temperature time series, and satellite-derived surface currents are made in section 6. In section 7 we summarize our methods and conclusions.

2. Data

The CPIES provide time series of bottom pressure, near-bottom current, and bottom-to-surface round-trip acoustic travel time. CPIES current meters are cabled 50 m above the bottom, a level designed to measure geostrophic current outside the bottom boundary layer (see discussion in section 3d and section 6). Sampling is 30 min for bottom pressure, hourly for current, and four pings every 10 min for travel time. Daily-averaged data were downloaded via acoustic telemetry on annual cruises, also allowing for servicing of malfunctioning instruments. Here we use the full data records extracted directly from the instruments after recovery.

CPIES data processing followed the procedures described in Tracey et al. (2013). Travel time τ and bottom pressure and velocity p, u, v are quality controlled by removing τ outliers and pressure spikes and steps. The τ outliers and pressure spikes are associated with unexpectedly strong bottom currents, causing an instrument to tip over for a period of time (all instruments self-righted when currents decreased). Some instruments were also dragged downslope by strong currents, causing an abrupt offset to higher pressure (pressure "step"). Travel time data are windowed and averaged to hourly values (Kennelly et al. 2007; Tracey et al. 2013). Currents are measured with an Aanderaa acoustic Doppler current sensor, and two corrections were applied. First, current directions were corrected for local magnetic declination. Second, current speeds were multiplied by a sound speed scale factor, the ratio of the local sound speed to the nominal value of 1500 m s^{-1} used by the instrument in situ. Bottom pressure is averaged to hourly, detided using response analysis (Munk and Cartwright 1966), and leveled and dedrifted using geostrophic streamfunction from geostrophic objective mapping of bottom velocity (Donohue et al. 2010). As described in Baker-Yeboah (2008) and Baker-Yeboah et al. (2009), τ is adjusted for (i) pathlength changes as determined by bottom pressure, (ii) the estimated inverted barometer effect of atmospheric pressure, (iii) the effect of latitude on gravity in converting between geometric height and pressure, and (iv) the seasonal cycle. It is then converted to travel time τ_{index} between the surface and an index level, here 2000 dbar, by fitting to $\tau_{\text{index}} = A\tau^2 + B\tau + C$, where coefficients A,

B, and C are depth dependent and determined empirically from historical hydrography, with additional adjustments to C based on CTD profiles taken at each site during CPIES sampling (Meinen and Watts 1998; Baker-Yeboah 2008; Baker-Yeboah et al. 2009; Donohue et al. 2010). The depth chosen for the index level is a compromise between a level deep enough to capture most of the travel time variability and one shallow enough to retain a large number of historical hydrographic profiles extending at least to that level. All data are then low-pass filtered using a fourth-order Butterworth filter with a 3-day cutoff, run forward and backward, and then subsampled to 0.5 day (with the first and last days removed to avoid transients). At each site for each variable, a single 4-yr-long time series is constructed. For instruments that were replaced during the experiment, a 4-yr-long time series is patched together from multiple deployments at the same site. These time series of twice-daily τ_{index} and bottom p, u, v are the inputs to objective mapping (in the following sections, we will use τ for τ_{index}).

Available CTD and Argo profiles within Drake Passage have been used to compute the cDrake GEMs for temperature, salinity, specific volume anomaly, and geopotential anomaly. Profiles for the cDrake GEM were taken from the geographic region spanning 54.5°–64.5°S and 57°–80°W (the top-right panel of Fig. 1) and were collected between 1975 and 2011. All 599 profiles extended to at least 2000 dbar, and 231 of them reached to 3800 dbar, below which the number of casts dropped off sharply. Most of the deep-reaching CTD casts (227) were collected on the five cDrake cruises between 2007 and 2011. In addition, 291 expendable CTD (XCTD) profiles (Sprintall et al. 2012) were used to estimate the seasonal cycle in the upper 150 m (Cutting 2010). The construction of the GEMs is described in appendix A. The GEMs are used to convert from CPIES τ_{index} to profiles of hydrographic properties.

A total of 99 full-depth lowered acoustic Doppler current profiler (LADCP) casts were made in the LDA on the five cDrake cruises. We excluded 27 casts that did not fall within half a day of available CPIES mapped data at the corresponding cast site (this excludes a number of the deployment and all of the recovery cruise casts, performed when fewer LDA CPIES were in the water), as well as 20 casts from the 2008 cruise, which had long midcast stops. Four more casts were excluded due to data processing issues. We compare velocity profiles from the remaining 48 LADCP casts with the corresponding cDrake velocity profiles interpolated to the location and time of each cast. The LADCP is a 153.6-kHz broadband RD Instruments ADCP, with a 30° beam angle and a 16-m vertical bin, pulse, and blank before transmit. Data were processed following the inversion method of Visbeck (2002) as updated by A. Thurnherr at Lamont-Doherty Earth Observatory (LDEO), using bottom-tracking, GPS-based ship drift, and shipboard ADCP velocities as constraints. Errors in velocity using this processing method have been estimated by Thurnherr (2010) as $<3\,\text{cm}\,\text{s}^{-1}$. Up- and downcast and cast-averaged velocity profiles computed in approximately 15-m depth bins are linearly interpolated to 20-m vertical resolution. For this work the barotropic tide as predicted by the Oregon State University Ocean Topography Experiment (TOPEX)/Poseidon Cross-Over Global Inverse Solution, version 7.2 (TPXO7.2), tidal model (Egbert et al. 1994) was removed.

Two current meter moorings deployed in Drake Passage as part of the Drake experiment (Ferrari et al. 2012) overlapped with the cDrake experiment in space and time. Mooring M2, located in 3800-m depth approximately 16 km from cDrake site C03 (Fig. 1), overlapped with cDrake for 11 months. Mooring M4, located in 4100-m depth approximately 5 km from cDrake site E02 in the LDA (Fig. 1), overlapped with cDrake for 16 months; M4 was turned around with new instruments 4.5 months into the overlap period. Each mooring collected current, temperature, and pressure observations at three depths. M2 had two Aquadopps and a rotor current meter 8 (RCM-8) at minimum pressures (representing full mooring extension) of 420, 930, and 2000 dbar, respectively. For the first deployment, M4 had an RCM-7, RCM-8, and RCM-11 at minimum pressures of 430, 960, and 2450 dbar, respectively; for the second deployment, RCM-11s were located at minimum pressures of 520, 1020, and 2540 dbar. Data from collocated microCATs and from an Aquadopp nominally at 500 m on M4 during the first deployment are not discussed here. Processing, described by Ferrari et al. (2012), includes correcting velocity data for local magnetic declination, daily averaging of both current and temperature data (collected at 2-hourly or shorter intervals), and correction for the effects of mooring motion using the method of Cronin and Watts (1996). We applied a 3-day low-pass filter to the daily current and temperature time series, to match the treatment of cDrake data (see above). Current outliers with either component larger than $1\,\text{m}\,\text{s}^{-1}$ were removed and replaced by linear interpolation before 3-day low-pass filtering. Because both rotor and acoustic velocity measurements may be affected by excessive instrument tilts, we excised velocity measurements at all three levels during intervals of large mooring drawdown, by removing the data on days when the 3-day low-pass-filtered pressure at the top instrument was more than 250 dbar greater than its minimum value. We compared both the mooring-motion-corrected and pressure-varying moored current and temperature records with cDrake current and temperature.

Here we show the most direct comparison, between the original pressure-varying moored records and cDrake currents and temperatures at the same varying pressures, which validates the cDrake fields.

We also compare cDrake surface currents with satellite surface currents derived from the mean absolute dynamic topography (MADT) produced by Segment Sol multimissions d'ALTimétrie, d'Orbitographie et de localisation précise (SSALTO)/Data Unification and Altimeter Combination System (DUACS) (http://www.aviso.oceanobs.com/en/data/product-information/duacs.html) and distributed by Archiving, Validation, and Interpretation of Satellite Oceanographic data (AVISO) with support from the Centre National d'Études Spatiales (CNES) (http://www.cnes.fr). We use the weekly delayed-time MADT, which incorporates sea level anomaly from multiple satellites (up to four at a time) with the CNES–Collecte Localisation Satellites 09 (CLS09) mean dynamic topography, on a 1/3° Mercator grid.

3. Computation of streamfunction and its derivatives by objective mapping

We objectively map from geopotential height anomaly Φ to baroclinic streamfunction and its derivatives, assuming geostrophy and a Gaussian covariance function for streamfunction ψ. Similarly, we map bottom p, u, and v to barotropic streamfunction and its derivatives. Some details of the implementation of objective mapping and calculation of vertical profiles of velocity and its derivatives for the cDrake LDA are laid out here.

a. Overview and motivation: Resolution and error estimation

We wish to calculate terms of the momentum and vorticity balances, including terms up to first derivatives of the relative vorticity $\zeta = v_x - u_y$, which require third derivatives of streamfunction. The algorithms for objective mapping to streamfunction, velocity, vorticity, and vorticity gradients are described in appendix B and below. Tests on a sample field meant to simulate the main eddy scale observed in the cDrake LDA (section 4) validated the fields and error estimates produced by these algorithms. The method of direct optimal mapping of derivatives was also compared to finite differencing of the velocity fields mapped on a 10-km grid. Finite differencing produces slightly noisier estimates, only notably worse for small residual quantities like divergence estimated as $u_x + v_y$. A further advantage of direct objective mapping, however, is that it provides a straightforward way to account for correlations in error estimates, which results in much smaller error estimates, closely aligned with the actual differences between analytic and mapped fields in the simulations. Similarly, a comparison of cDrake velocity fields with moored velocities (section 6a) indicated that the direct mapping error estimates (see sections 3e and 5) corresponded to the differences between cDrake and moored velocities and shears. By comparison, the uncertainties derived by propagation of error in finite-differenced $d\Phi/d\tau$, which did not account for correlations, overestimated the actual errors by factors of 2–4. For this reason, we convert measured τ_{index} to Φ as described in appendix A, and then objectively map to Φ and its derivatives at selected pressure levels (here, every 200 dbar).

TABLE 1. Mapping parameters for the indicated quantities and time series. For Φ, we use L_τ and $E_\Phi = E_\tau + E_{\text{GEM}}(p)$ (see section 3c).

	L (km)	E
Mean	200	0.15
p, u, v LP	60	0.25
p, u, v HP	50	0.35, 0.46 (p tip step)
τ LP	60	0.04
τ HP	50	0.09

b. Background means, multiple scales, and mapping parameters

The fields we wish to map contain multiple time and space scales; we follow a multistep, multiscale procedure in order to capture as much of the variance as possible. We first describe the steps, followed by the method used to obtain the covariance length scales (L) and data noise-to-signal variance ratios (E), given in Table 1, from the observations. Each step operates on streamfunction (Φ or scaled bottom p) and, where available, velocity multiplied by the Coriolis parameter (fu, fv). For baroclinic streamfunction we map $\psi(x, y, t) = \Phi(p_i, x, y, t)$ separately for each pressure level p_i (Φ is relative to 4000 dbar). For the barotropic reference streamfunction, we map $\psi = p/\rho_0, fu, fv$ ($\rho_0 = 1050\,\text{kg m}^{-3}$) derived from the bottom-measured p, u, v.

For the first mapping step for each desired variable θ, the time mean(s) (denoted by angle brackets) are mapped at a large scale, producing $\widehat{\langle\theta\rangle}$. For the second step, the twice-daily data with this time-mean map removed are filtered (see below) to produce the low-pass-filtered (LP) time series θ_{LP}, which are mapped at each time step using a shorter scale (see Table 1), producing $\hat{\theta}_{\text{LP}}$. The LP and time-mean maps are then subtracted from the twice-daily data to produce the high-pass-filtered (HP) time series θ_{HP}, which are mapped at each time step with an even smaller scale (Table 1), producing $\hat{\theta}_{\text{HP}}$. Finally, the time mean, LP, and HP maps are summed as shown:

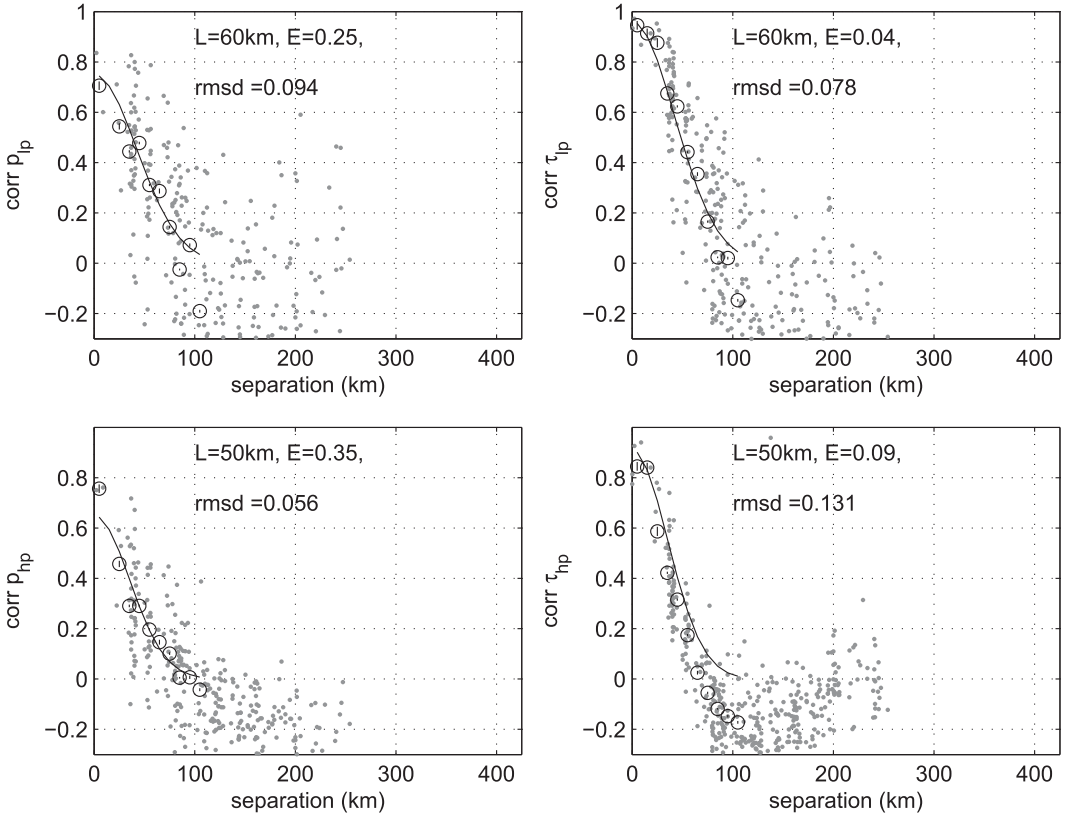

FIG. 2. (left) Pressure–pressure and (right) τ_{index}-τ_{index} correlations (gray dots) between pairs of sites, plotted as a function of site separation, for (top) LP and (bottom) HP series. Bin-averaged correlations c_{bin} are plotted as black circles and the best-fit Gaussian, c_g, as a black curve. The τ_{index} is the round-trip acoustic travel time between 0 and 2000 dbar.

$$\hat{\theta} = \widehat{\langle\theta\rangle} + \hat{\theta}_{\text{LP}} + \hat{\theta}_{\text{HP}}. \tag{1}$$

The objective mapping procedure (Bretherton et al. 1976) assumes input fields with zero mean, so at each mapping step we remove the spatial mean from the streamfunction before mapping. In cases where velocity is an input to mapping, we also remove the spatial means $\overline{u}$, $\overline{v}$ from u, v, and the corresponding plane $f\overline{v}x - f\overline{u}y$ from streamfunction. After each mapping step, the spatial mean(s) (and plane, if applicable) are added back to the mapped streamfunction and velocity. The baroclinic and barotropic (bottom reference) fields are combined after mapping (see section 3d below).

For the division into LP and HP time series, we use a Butterworth filter with a cutoff period of 61 days, chosen to keep the LP and HP velocity variances approximately equal. For the time-mean, large-scale map we use a decorrelation scale of $L = 200$ km and a data noise-to-signal ratio of $E = 0.15$. For both LP and HP, we determined optimal L and E by calculating correlations between all pairs of sites independently for both τ and pressure observations. Correlations for all pairs are plotted as a function of separation distance in Fig. 2. A Gaussian

$$c_g = (1 - E)e^{-r^2/L^2} \tag{2}$$

was least squares fitted to the correlations $c_{\text{bin}}(r)$ averaged to 10-km r bins (Fig. 2) by varying L and E. The parameters for mapping bottom p and τ are given in Table 1. The correlation lengths L obtained for bottom p were also used for bottom u and v in their respective derivative correlation functions. Since Φ is generated from τ using the GEM lookup table (appendix A), we use L_τ and $E_\phi = E_\tau + E_{\text{GEM}}$ to incorporate the observed Φ scatter relative to the GEM in the calculation. The calculation of E_{GEM} is described below. Details of the computation of L and E, including an increased estimate of input measurement error arising from CPIES tipping events and level changes (discussed in section 2) at six sites (Fig. 1) by using a site-dependent E, are given in Firing (2012).

Upon examination of the velocity records and the high-resolution bathymetry obtained during the project,

we found that site B02 (Fig. 1) was situated in a narrow canyon and has elongated velocity variance ellipses parallel to the canyon axis, suggesting that the near-bottom flow was constrained by the local bathymetry rather than representing the larger-scale pressure gradients. We have excluded currents from this site from the geostrophic objective mapping of bottom p, u, v.

The spatial resolution of the cDrake CPIES observations was sufficient to construct mapped fields at each time step without the need for inputs from other time steps. Interpolation in time was also unnecessary for mapping the mesoscale field at time scales of 3 days and longer, starting from twice-daily CPIES observations at each site. Thus, the cDrake mapping only uses spatial correlation length scales; temporal correlations were not incorporated.

c. The Φ GEM-derived contribution to noise-to-signal variance for objective mapping

The specific volume anomaly GEM ($\delta_{\rm GEM}$) is constructed by fitting smoothing-spline curves to a set of CTD-derived specific volume anomaly values $\delta_{\rm CTD}$ (see appendix A) and then interpolating the fitted splines to 10-dbar vertical resolution. To estimate the contribution to Φ error from this process, we calculate $\Phi_{\rm CTD}$ by integrating $\delta_{\rm CTD}$ and $\Phi_{\rm GEM}$ by integrating $\delta_{\rm GEM}$. We take the deviation from the GEM to represent the noise and the GEM itself to represent the signal, so that we have

$$\sigma_n^2(p) = \frac{1}{N_{\rm CTD}(p)-1}\sum_{i=1}^{N_{\rm CTD}}[\Phi_{{\rm CTD},i}(p) - \Phi_{\rm GEM}(p,\tau_{{\rm CTD},i})],$$

$$\sigma_s^2(p) = \frac{1}{N_{\rm GEM}(p)-1}\sum_{j=1}^{N_{\rm GEM}}[\Phi_{\rm GEM}(p,\tau_j) - \overline{\Phi_{\rm GEM}(p)}]^2,$$

$$E_{\rm GEM} = \sigma_n^2/\sigma_s^2, \tag{3}$$

where $N_{\rm CTD}$ is the number of CTD samples at each pressure level, $\tau_{{\rm CTD},i}$ is the $\tau_{\rm index}$ of the ith CTD profile, and $N_{\rm GEM}$ is the number of $\tau_{\rm index}$ bins in the GEM. We included only the 524 CTD profiles with $\tau_{\rm index}$ within the range observed in the LDA over the 4 years of cDrake. We take $E_{\rm GEM}$, which varies from 0.02 at the surface to 0.30 at 3800 dbar, to be the GEM contribution to the noise-to-signal ratio for mapping Φ. We partition $E_{\rm GEM}$ between the LP and HP components of Φ according to their relative variances.

d. Adjustment for deep shear in leveling pressure and mapping barotropic fields

To dedrift and level the bottom pressure data, measured pressure records are compared to mapped pressure based on objective mapping of near-bottom currents. Mapping near-bottom currents, measured at depths ranging from 3500 to 4300 m in the LDA, as though they were all measured at one level, relies on the assumption of negligible deep shear. Mapped Φ gradients in the 3500–4300-dbar range have an rms vertical shear of $<2\times10^{-4}\,{\rm s}^{-1}$, with mean values an order of magnitude smaller. We therefore account for deep geostrophic shears by an iterative procedure. Bottom currents are first mapped as though they were all measured at the same level, and the maps are used to dedrift and level pressure records. The resulting dedrifted, leveled pressures are used to correct τ, as described in section 2 and Tracey et al. (2013). Shear derived from this τ is then used to adjust near-bottom current measurements from the estimated instrument depths to 4000 dbar before mapping, and the pressure dedrifting and leveling is redone using these adjusted current maps. While the effect of this correction on the maps is small, we will use the shear-adjusted fields from here on; references to ''bottom'' p, u, v from section 3b onward are to these adjusted values. The ''barotropic'' fields produced by mapping the 4000-dbar-adjusted p, u, v are then used to reference the baroclinic fields at 4000 dbar.

The CPIES near-bottom current meters (tethered 50 m above the seafloor) may at times be within the bottom boundary layer, leading to measurements affected by ageostrophic shear. The previously estimated bottom boundary layer thickness of ≤50 m holds for current speeds up to $0.38\,{\rm m\,s}^{-1}$ [Csanady (1967), assuming a drag coefficient of $c_d = 1.5\times10^{-3}$]. Speeds measured hourly by the CPIES current meters in the LDA exceed this level only 3% of the time, implying that the CPIES near-bottom current measurements are only rarely influenced by the bottom boundary layer. Direct application of such measurements as bottom reference velocities for the τ-derived baroclinic velocity profile would affect the total velocity profile as follows. Application of bottom Ekman layer currents, rotated clockwise compared to the true deep geostrophic reference velocity, would generally produce total currents also rotated clockwise of their true values. However, in cases of sufficiently strong baroclinic shear directed counterclockwise of the deep currents, the application of bottom Ekman layer currents attenuated (as well as rotated) relative to the true deep geostrophic reference would produce total currents rotated counterclockwise of their true values. The objective mapping procedure, however, mitigates the effect of any velocity measurements made within the bottom boundary layer by incorporating the bottom pressure measurements as well. In fact, as noted in section 6, we find that where angle biases between cDrake mapped currents and independent

measurements are observed, they are not generally consistent with the expected ageostrophic bottom boundary layer effects, implying that these are of, at most, occasional and localized importance.

e. Mapping error estimates

The objective mapping algorithm (Bretherton et al. 1976) also provides for estimation of the percent error variance, $e_{\hat{\theta}}(x,y,t)$, for each estimate $\hat{\theta}(x,y,t)$ of a quantity $\theta(x, y, t)$; $e_{\hat{\theta}}(x,y,t)$ depends on the relative location of all input data and on the covariance function and its length scale L and input noise-to-signal ratio E. To combine errors from mapping at different scales and to estimate propagation of error when computing other quantities from mapped fields, we seek the dimensional error variance. The percent error variance is normalized by the signal variance $\sigma_\theta^2 = \overline{\theta^2}(x,y)$, the diagonal of the covariance matrix used in the mapping (appendix B), so the dimensional error variance is just $e_{\hat{\theta}}(x,y)\sigma_\theta^2$. We estimate the signal variance from the mapped fields as $\sigma_\theta^2 \simeq \sigma_{\hat{\theta}}^2 = \langle \overline{\hat{\theta}(x,y,t)^2} \rangle$, where the overbar indicates a space mean and the angle brackets a time mean [recall that $\overline{\theta(x,y,t)} = \overline{\hat{\theta}(x,y,t)} = 0$]. Anisotropy between different derivatives of the same order is small, so we also average the variance estimates from different derivatives (σ_u^2 and σ_v^2, for instance) and use a single signal variance factor for each derivative order. The total dimensional error variance for each mapped variable θ in Eq. (1) is

$$e_{\langle\hat{\theta}\rangle}\sigma^2_{\langle\theta\rangle} + e_{\hat{\theta}_{\mathrm{LP}}}\sigma^2_{\theta_{\mathrm{LP}}} + e_{\hat{\theta}_{\mathrm{HP}}}\sigma^2_{\theta_{\mathrm{HP}}}. \tag{4}$$

Maps of error for cDrake fields are discussed in section 5.

f. Sensitivity to mapping parameters

We tested the sensitivity of the objective mapping to variations of 20% in L and E by comparing streamfunction first derivatives (u, v), second derivatives (ζ), and third derivatives ($\nabla\zeta$) with modified parameters to the same quantities from mapping with the parameters given in Table 1. Comparisons were restricted to the good mapping region (Fig. 1). Results of the comparisons, in terms of normalized rms differences and correlations, are given in Table 2 (mean differences are not shown but are negligible in all cases). All maps produced with modified parameters are well correlated ($r > 0.9$) with maps produced with original parameters. The choice of parameters has the least effect on the velocity maps (differences of 5%–20%) and the largest effect on the vorticity gradient maps (differences of 11%–63%). All maps are most sensitive to variations in L_{HP}, with the largest effects coming from decreased L_{HP}, which produces maps with significantly larger extrema. The large sensitivity of third-derivative estimates is not surprising, given that the LDA instrument spacing is approximately 37 km—not much shorter than the optimal L_{HP} (50 km; see Table 1).

TABLE 2. Comparisons of streamfunction derivatives obtained by objective mapping with indicated parameters (L, E) increased or decreased by 20% relative to their values given in Table 1. The two metrics in each box are the maximum rmsd normalized by the spatial standard deviation of the original map, and the minimum correlation. The variable $\Phi(0)$ indicates Φ at the surface; surface $E_\Phi \simeq E_\tau + 0.02$. The comparisons include only mapping grid points within the good mapping region (Fig. 1).

	L_{LP}	L_{HP}	E_{LP}	E_{HP}
u, v from p, u, v	0.10, 0.99	0.20, 0.98	0.04, 1.00	0.05, 1.00
u, v from $\Phi(0)$	0.14, 0.99	0.15, 0.99	0.01, 1.00	0.03, 1.00
ζ from p, u, v	0.17, 0.99	0.37, 0.95	0.06, 1.00	0.07, 1.00
ζ from $\Phi(0)$	0.17, 0.99	0.23, 0.98	0.04, 1.00	0.07, 1.00
ζ_x, ζ_y from p, u, v	0.26, 0.98	0.63, 0.91	0.08, 1.00	0.11, 1.00
ζ_x, ζ_y from $\Phi(0)$	0.27, 0.97	0.41, 0.95	0.05, 1.00	0.09, 1.00

4. Mapping idealized fields to estimate momentum and vorticity advection

We describe the mapping of idealized analytic fields in order to validate the capability of the cDrake objective mapping procedure described in section 3 to produce higher derivatives of the input fields and to verify that the dimensional error estimates (section 3e) accurately capture the uncertainty as determined by deviation from the analytic fields. We chose the analytic fields to model observations in the LDA, using a streamfunction characterized by near-isotropic highs and lows with wavelength approximately the length of the array, propagating through the array over a period of 30 days in approximately the same direction as the mean flow.

The analytic streamfunction and velocity combine a constant jet with propagating meander or "eddy" variability:

$$\psi = \frac{ak_e}{k_j}\sin[k_j(y-y_{0j})] + a\cos[k_e(y-y_0)] \times \cos\{k_e[x-x_0(t)]\}, \tag{5}$$

$$f_0 u = ak_e\cos[k_j(y-y_{0j})] + ak_e\sin[k_e(y-y_0)] \times \cos\{k_e[x-x_0(t)]\}, \tag{6}$$

$$f_0 v = -ak_e\cos[k_e(y-y_0)]\sin\{k_e[x-x_0(t)]\}, \tag{7}$$

with $a = U_0 f_0/k_e$, jet and eddy amplitude $U_0 = 0.3\,\mathrm{m\,s^{-1}}$, a constant Coriolis parameter $f_0 = 2\Omega\sin(-57°)$, $\Omega = 7.292 \times 10^{-5}\,\mathrm{s^{-1}}$, eddy wavenumber $k_e = 2\pi/(200 \times 10^3)\,\mathrm{m^{-1}}$, jet wavenumber $k_j = 2\pi/(220 \times 10^3)\,\mathrm{m^{-1}}$,

$y_{0,j} = 60 \times 10^3$ m, $y_0 = 10 \times 10^3$ m, $x_0(t) = 2\pi t/(Tk_e)$, and an eddy period of $T = 30$ days. The analytic fields were subsampled on a 40-km, 3×7 grid (Fig. 3) over $t = 1, 2, \ldots, 10T$ days. We added to each variable (ψ, u, v) noise from a random, zero-mean normal distribution with variance $(n\sigma_\psi^2, n\sigma_v^2, n\sigma_v^2)$, where $\sigma_\psi^2 = a^2k_e^2k_j^{-2}/2 + a^2/4$ and $\sigma_v^2 = a^2k_e^2/4$ are the space variances of the analytic ψ and v fields (note that σ_v^2 is also the variance of the eddy part of the u field; the u and v fields were assigned equal noise variance, proportional to this eddy variance). Values for n ranged from 0.05 to 0.35. To model noise correlated over T_n days, we linearly interpolated from random noise fields every T_n days to the intervening days (if any); we tested T_n from 1 to 15 days.

At each time we mapped the subsampled ψ or ψ, u, v, using the same procedures as for cDrake (described in section 3 and appendix B), to ψ and its first, second, and third derivatives on a 10-km grid. The mapping noise-to-signal variance E for (ψ, u, v) was set to $(n, n\sigma_v^2/\sigma_u^2, n)$, where $\sigma_u^2 = a^2k_e^2/4 + a^2k_j^2/2$. The mapping decorrelation length was $L = 60$ km. As described in section 3b, a mean over the 21 input sites was subtracted from ψ before mapping each day, and in the case of mapping from ψ, u, v, means were subtracted from u, v, and the corresponding plane from ψ. We also estimated the dimensional error variance as in section 3e, using the analytic field variances σ_θ^2 to redimensionalize percent error variance $e_{\hat{\theta}}$.

We compare both day-by-day and time-averaged fields and error fields. Time averages were calculated over $T/2$, assuming each day to be independent. To improve the statistics of the error comparisons, we used multiple ensembles of $T/2$ days. We test the accuracy of both the mapped fields themselves (section 4a) and the estimates of error in the mapped fields derived from the objective mapping algorithm (section 4b).

a. Mapped–analytic field comparisons

Plan view plots of 15-day means (Fig. 3) show that objective mapping from ψ, u, v is able to reproduce mean analytic velocity, relative vorticity, and even relative vorticity gradients in the center of the array. Mapped and analytic variables are well correlated and of the same size, with relatively low scatter around a 1:1 relationship (rms differences for each quantity are indicated in the bottom-right corners of Fig. 3). In the region shown, the mapped mean field amplitudes for each variable exceed their respective estimated errors for all but the smallest values (not shown; see section 4b). As the input noise-to-signal variance and/or the noise correlation time is increased (up to $n = 0.35$, $T_n = 15$), the scatter between mapped and analytic quantities becomes larger. However, as error bars also increase with increasing n, the objectively mapped fields still reproduce the analytic fields in the central area to within predicted error (see below). Mapping from ψ alone produces qualitatively similar results to mapping from ψ, u, v, with rms analytic–mapped differences approximately twice as large.

b. Error estimate comparisons

As described in section 3e, for each mapped quantity θ and mapping estimate $\hat{\theta}$, the dimensional error variance for the objective maps can be computed as

$$\sigma_{\hat{\theta}}^2(\mathbf{x}) = e_{\hat{\theta}}(\mathbf{x})\sigma_\theta^2, \tag{8}$$

where σ_θ^2 is the analytic signal variance. We can also directly calculate the error variance from the mapped $(\hat{\theta})$ versus analytic (θ) simulation fields using

$$\delta_\theta^2(\mathbf{x}) = \langle [\theta(\mathbf{x}) - \hat{\theta}(\mathbf{x})]^2 \rangle, \tag{9}$$

where the angle brackets indicate averaging over realizations. We can now verify that $\sigma_{\hat{\theta}}^2(\mathbf{x})$ is a good predictor of $\delta_\theta^2(\mathbf{x})$. Comparisons of Eqs. (8) and (9) for a range of input parameters, averaging over $10T$ (or $20\,T/2$ ensembles), for ψ and its first and second derivatives as well as ζ, ζ_x, ζ_y show good agreement between the two methods. The rms mapping error (rmse, black lines in Fig. 4) is a good approximation to the standard deviation of the scatter of the mapped values around the analytic line [rms differences (rmsd) in Fig. 4].

Estimates of error on mean quantities can also be compared: the standard error of the mean estimated by propagation of mapping error-based variances, calculated using

$$s_m = \frac{\sqrt{\langle \sigma_\theta^2 \rangle}}{\sqrt{N}}, \tag{10}$$

with N equal to the number of estimates, should be the standard deviation of the distribution of

$$\Delta = \langle \theta \rangle - \langle \hat{\theta} \rangle. \tag{11}$$

We computed 20 sets of 15-day averages for various input parameters for the fields discussed above. The widths of the best-fit zero-mean Gaussians for Δ are a factor of 1–2 times the rms(s_m) for all variables, confirming the accuracy of the mapping error estimates.

c. Momentum and vorticity tendency and advection

The ultimate goals of the methods described here are to objectively map velocity, velocity gradients, vorticity, and vorticity gradients in order to estimate terms of the

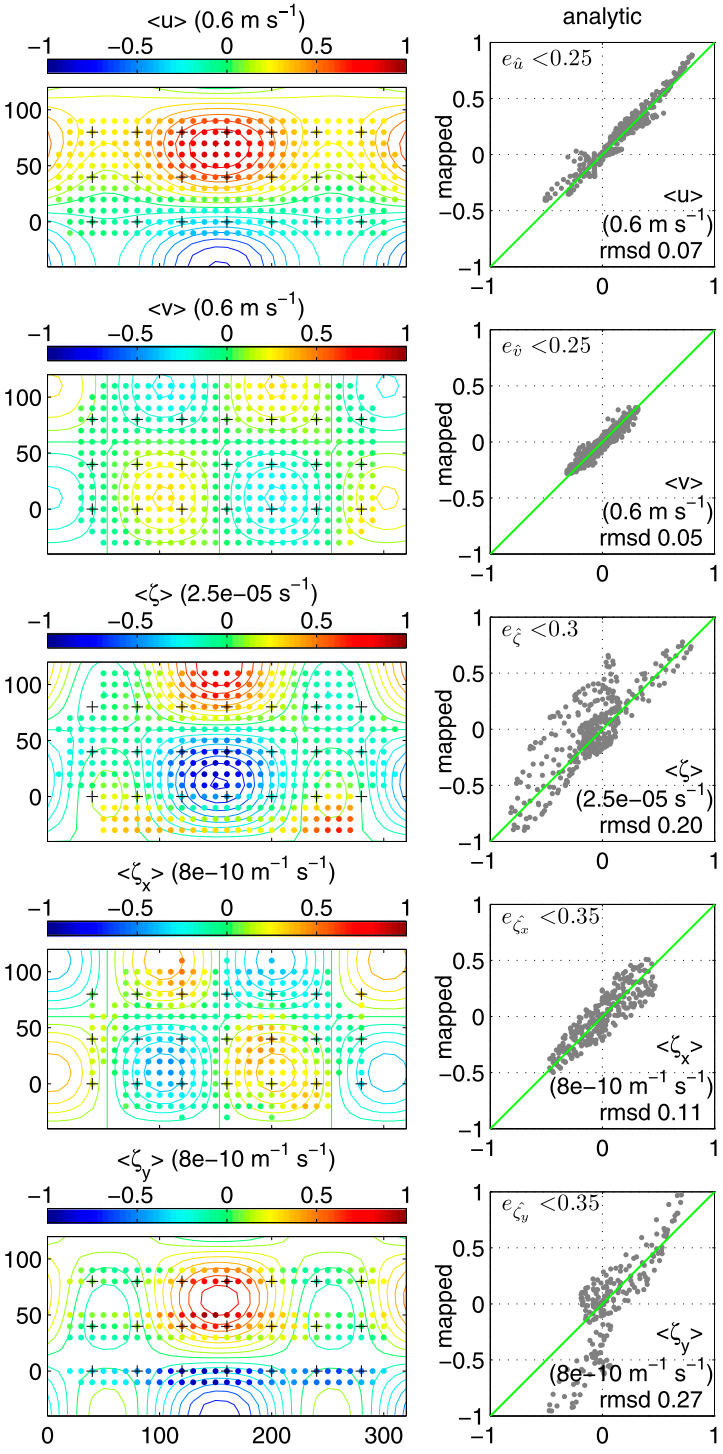

FIG. 3. 15-day mean velocity components, relative vorticity, and relative vorticity gradient components mapped from ψ, u, v with $n = 0.20$, $T_n = 7$. (left) Analytic (contours) and mapped (dots). (right) Analytic vs mapped values for the same quantities (gray dots), with the 1:1 line shown in green. Color bars and axes have been normalized to $[-1, 1]$; scale factors and units are given above the color bars and on the bottom right of each right-hand plot. The (normalized) rmsd, with the same scale as other plot quantities, are also given. The percent error variance criterion for points plotted in both left- and right-hand panels is shown in the top-left corner of each right-hand plot.

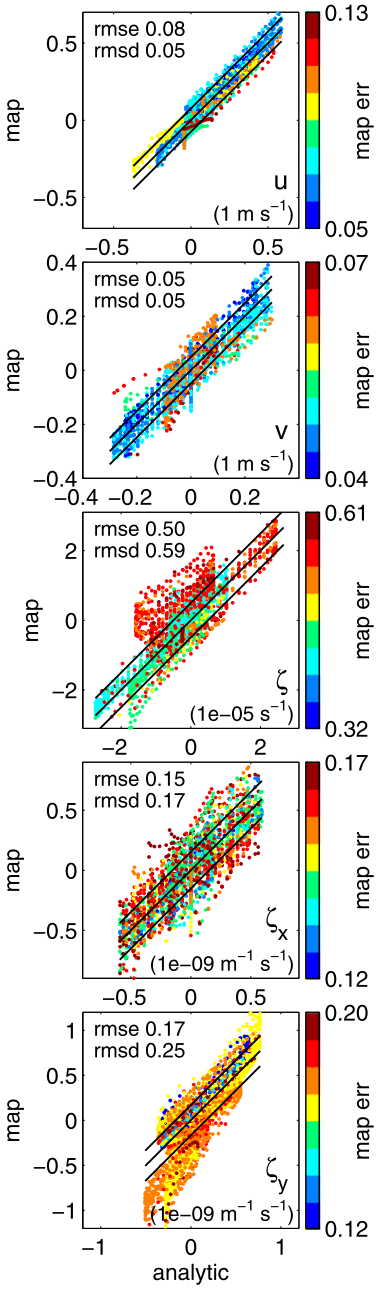

FIG. 4. Scatterplots of 15 days of daily analytic vs mapped values for (top to bottom) u, v, ζ, ζ_x, ζ_y. Only points with daily percent variance mapping error $e_{\hat{\theta}}$ meeting the cutoffs given in Fig. 3 are shown. The color of each point corresponds to the mapping error $\sigma_{\hat{\theta}}$ at that point, as indicated by the color bar. The black lines are the 1:1 line and 1:1 ± the rms of mapping error (rmse); the rmsd δ is also given. In general, low predicted error corresponds to good agreement between mapped and analytic values, and overall rmse values describe the scatter of the mapped values about the analytic (as indicated by the black lines). Scales in the bottom-right corner of each panel apply to the axes and color bar labels as well as rmse and rmsd.

momentum and vorticity balances, including nonlinear advection terms, from the cDrake observations. Having demonstrated above the reproduction by objective mapping of the simulated analytic velocity, vorticity, and vorticity gradient fields, and the production of accurate error estimates for these fields, we compare the analytic time series of momentum and vorticity balance terms with the corresponding time series, with uncertainties, based on mapped fields.

Mapped time series of zonal momentum balance terms (Fig. 5) from points near the center of the array reproduce the signs, slopes, curvatures, and relative sizes of the analytic time series, despite the noise ($n = 0.20$, $T_n = 7$) in the mapped data. With smoothing by a 4th order Butterworth with a 7-day cutoff period, the correspondence is even clearer. Moreover, when this smoothing is incorporated, the comparison between mapped and analytic momentum balance terms in the central area is as good from mapping from ψ alone for the baroclinic field (not shown) as it is from mapping from ψ, u, v for the deep reference field (Fig. 5).

Vorticity balance terms (Fig. 6) are noisier, but a consistent picture arises when the terms are smoothed with a 7-day Butterworth filter. After smoothing, time series mapped from ψ, u, v reproduce the signs and relative amplitudes of $u\zeta_x$, $v\zeta_y$, and ζ_t with n up to 0.35 and T_n up to 15 days. If mapped from ψ only, signs and amplitudes are reproduced with n up to 0.10 and T_n up to 7. The predicted error also indicates correctly the point at which the noise level becomes so large as to bury the signal.

d. *Summary of simulations*

Objective mapping has allowed us to reproduce simulated analytic streamfunction, velocity, vorticity, and vorticity gradients, and to accurately estimate the uncertainty on mapped fields. The tendency and nonlinear advection terms in the momentum and vorticity balances are also reproduced from the mapped fields, to within mapping-derived uncertainty. We infer from these simulations that diagnoses of momentum and vorticity balances should be successful using cDrake observations in the LDA.

5. cDrake fields and error maps

We estimated dimensional mapping errors, as described in section 3e, for twice-daily barotropic and baroclinic mapped fields. Errors on total fields are obtained by summing the barotropic and baroclinic error variances. Mapping errors are small in the region encompassed by the CPIES sites, and increase with distance outside the array. The cDrake baroclinic fields,

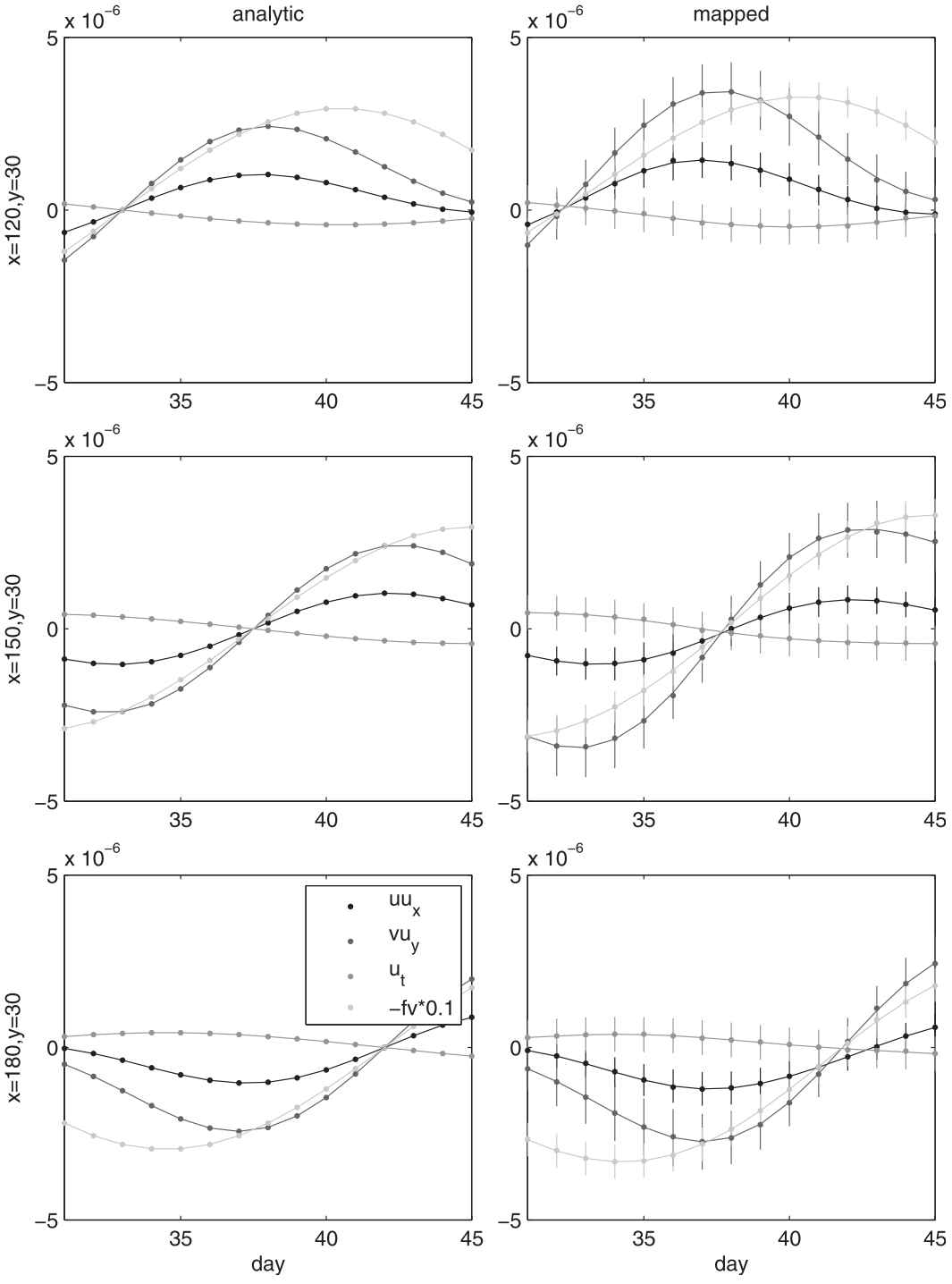

FIG. 5. (left) Analytic and (right) mapped time series of key zonal momentum balance terms ($\mathrm{m\,s^{-2}}$) at three representative points in the center of the array ($x = 120, 150, 180$; $y = 30$; note the central pluses in Fig. 3 are at $y = 40$). Daily data are shown by dots and data smoothed with a fourth-order Butterworth filter with a 7-day cutoff by solid lines. Vertical lines in (right) indicate standard deviation error bars on the smoothed data. Mapping was from ψ, u, v with $n = 0.20$, $T_n = 7$ (see text). The mapped tendency term, u_t, was estimated by center differencing. Note that the first-order balance is between the Coriolis term $-fv$ and the pressure gradient term (identical by construction).

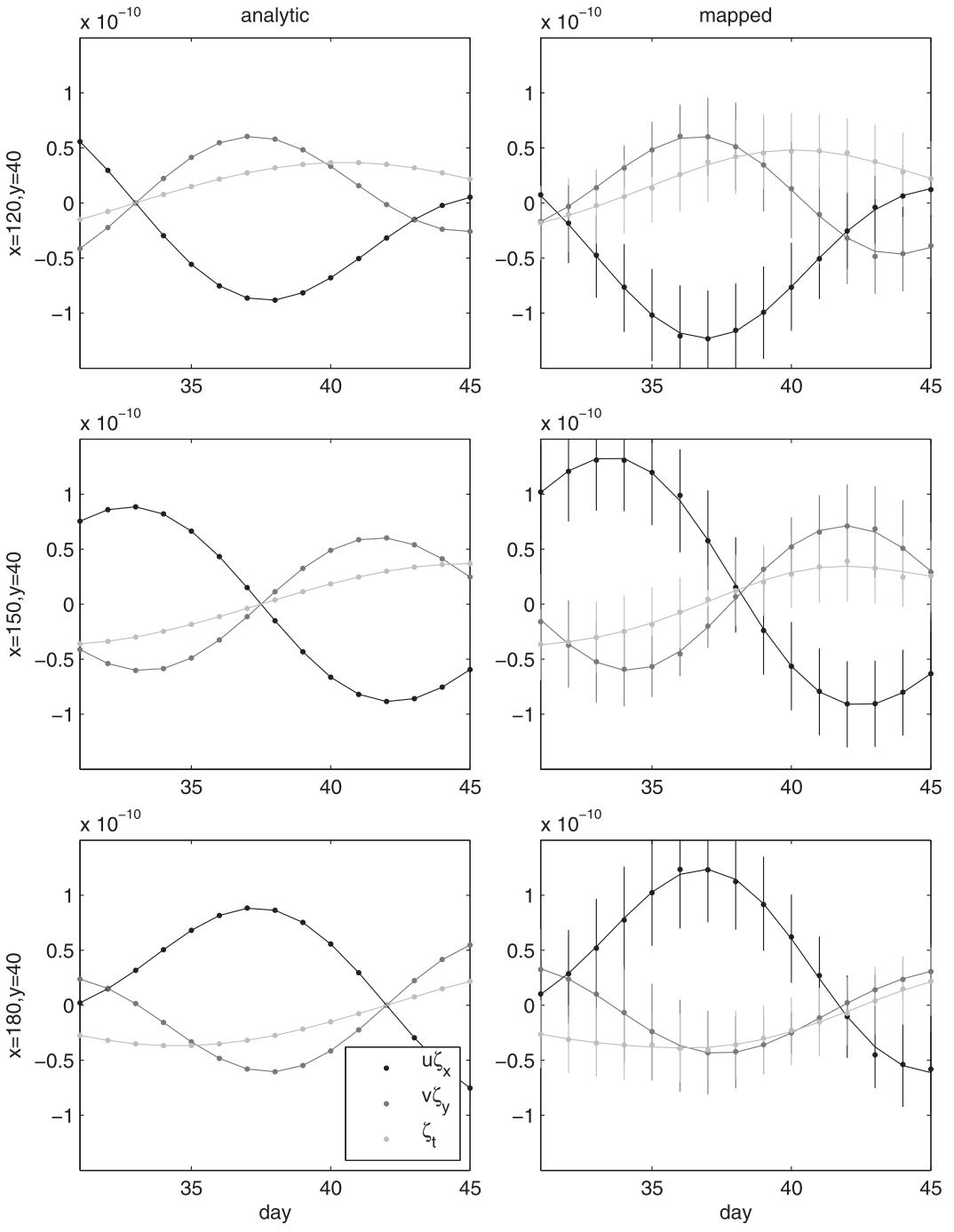

FIG. 6. As in Fig. 5, but for selected vorticity balance terms (s^{-2}).

which are mapped from geopotential anomaly (streamfunction) alone, have larger errors than barotropic fields, which are mapped from bottom velocity as well as pressure (streamfunction). For the cDrake baroclinic fields, although percent variance errors increase with depth, variance decreases faster, so that dimensional errors decrease with depth. Dimensional errors on baroclinic velocity, for example, are about 85% as large at 400 dbar as at the surface, 55% as large at 1000 dbar, and 2% at 4000 dbar. The good mapping region, shown in Fig. 1, surrounds the LDA CPIES sites and corresponds to the $e_{\hat{\psi}} < 0.13$ contour of the bottom map (from p, u, v). We have mapped both baroclinic and barotropic reference fields within this same good mapping region.

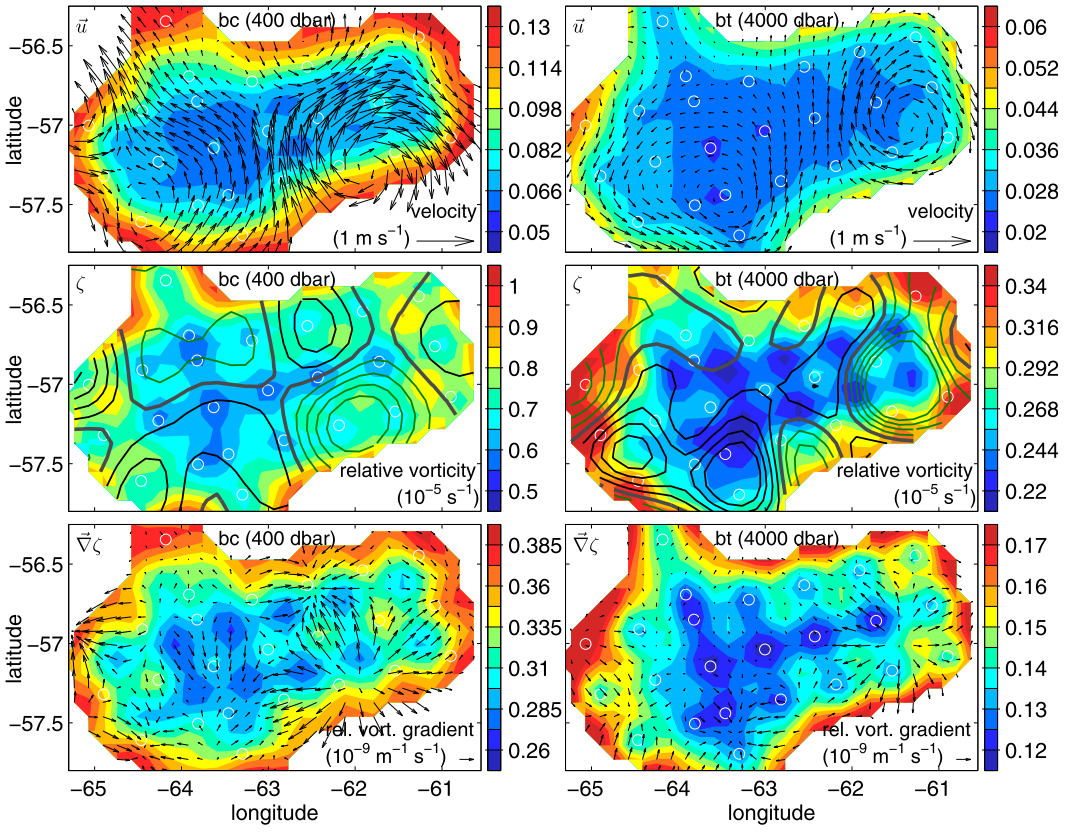

FIG. 7. Example of objectively mapped fields (vectors and line contours) and dimensional errors (filled color contours) within the good mapping region (Fig. 1) on a typical day (14 Feb 2008), showing baroclinic fields at 400 dbar and barotropic reference fields at 4000 dbar: (top) velocity **u**, (middle) relative vorticity ζ, and (bottom) relative vorticity gradient $\nabla\zeta$. For vector fields, the average vector component errors are shown. Scales in parentheses (bottom-right corners) apply to the color bar as well as to the adjacent scale vectors (in top and bottom panels). Relative vorticity is contoured every (left) 10^{-5} or (right) 0.33×10^{-5} s^{-1}, with thick gray contour = 0, green contours <0, and black contours >0. CPIES sites are marked by white circles. Note that errors on 4-yr mean fields are approximately 10 times smaller than the daily map errors shown here.

Typical dimensional error fields for twice-daily barotropic and baroclinic (at 400 dbar) velocity, relative vorticity, and relative vorticity gradients are shown in Fig. 7. The rms dimensional errors within the good mapping region are listed in Table 3 for both barotropic and baroclinic (at 400 dbar) streamfunction and specified streamfunction derivatives. The relative contributions of the three terms in Eq. (4) are as follows. For streamfunction and velocity, about 4% of the total error variance is contributed by the time-mean maps, while the 61-day LP maps contribute approximately 43% and the residual HP maps about 53%. For higher derivatives, the HP maps contribute about 70% of the total variance and the LP maps the remaining 30%; contributions to error from the time-mean fields are negligible.

Twice-daily streamfunction (not shown), velocity, and relative vorticity (Fig. 7) can be mapped with errors smaller than typical field values. Velocity component errors in the good mapping region are 40%–50% of the velocity spatial standard deviation, or about 20% of typical speeds in strong flow regions (e.g., the eddy shown in the eastern LDA in Fig. 7). Typical vorticity errors are 50%–60% of the vorticity spatial standard deviation, or approximately 20%–25% the size of typical vorticity maxima. Errors on vorticity gradient components (Fig. 7, bottom panels) are 70%–80% of the spatial standard deviations, nearly comparable in size to the twice-daily gradient fields themselves. Standard errors of the mean over the 4 years of cDrake, however, are smaller than the twice-daily errors by a factor of about 10 (based on the 11-day integral time scale of the cDrake time series), such that the time-averaged relative vorticity gradient signal in cDrake is larger than the uncertainty. The same is true for the nonlinear relative vorticity advection (not shown).

TABLE 3. Dimensional mapping errors for indicated cDrake mapped fields for 3-day low-pass-filtered time series. Values shown are rms over time and over the mapping grid points within the good mapping region (Fig. 1). Errors are given for the barotropic bottom reference field (ref subscript), the baroclinic field at a representative upper level, 400 dbar (bc subscript), and the combined total field at 400 dbar. The ref and bc errors are each the sum of the errors on the time-mean, 61-day LP, and residual HP mapped fields [see Eqs. (1) and (4)]. The error for the total field at 400 dbar is obtained by summing the ref and bc variances.

Field	$\hat{\theta}_{\mathrm{ref}}$	$\hat{\theta}_{\mathrm{bc}}$	$\hat{\theta}$
ψ ($10^{-1}\,\mathrm{m^2\,s^{-2}}$)	1.5	3.6	3.8
u, v ($\mathrm{m\,s^{-1}}$)	0.04	0.10	0.11
ζ ($10^{-6}\,\mathrm{s^{-1}}$)	3.2	8.0	8.7
ζ_x, ζ_y ($10^{-10}\,\mathrm{m^{-1}\,s^{-1}}$)	1.6	3.6	4.0

6. Comparison with independent datasets

In section 4 we investigated and confirmed the internal consistency of the cDrake mapping method using simulated data. Here we investigate the validity of the cDrake mapping and GEM-derived fields by comparison with independent observations. Comparison with coincident moored currents validates the time variability of the currents and current shear. The cDrake GEM-derived mean surface currents also compare well with mean (over the same time period) satellite altimeter MADT-derived surface currents over most of the LDA area. The LADCP comparison helps confirm the GEM-derived vertical structure.

a. Comparison with moored currents and temperature

The geostrophic currents mapped in the cDrake array are compared in this subsection to measurements of the full current at individual moorings. Some of the ageostrophic components contained in the moored measurements have been removed by 3-day low-pass filtering all time series; however, submesoscale spatial structures and gradient-balance terms remain and reflect real differences between these two types of current measurements, even if both were perfectly error free. The moored current meter and temperature measurements are from the Drake experiment moorings M2 and M4 (marked in Fig. 1). To compare with moored velocities at time-varying depths, we linearly interpolated the cDrake objectively mapped velocities to the nominal location of each mooring and to match the pressure time series $p(t)$ from each instrument. To compare with temperature, we interpolated the T GEM to $p(t)$ and $\tau(t)$ from cDrake maps at the mooring location. To estimate the standard error of moored time means, we multiplied their standard deviations by $1/\sqrt{N_{\mathrm{dof}}}$, where the number of degrees of freedom N_{dof} was the number of days in the time series divided by 11 days (the decorrelation time scale for cDrake mapped velocity). For cDrake, we can also incorporate information on the error of individual measurements (sections 3e and 5) by propagation of error. For the comparisons in this section, days on which mooring drawdown exceeded 250 dbar (see section 2) were excluded from both moored and cDrake velocity records.

M2 was located north of the LDA and 6 km west of the C line along the continental slope, 16 km from the nearest CPIES (C03; Fig. 1). Although it is not in the two-dimensional LDA mapping region, we can compare the temperatures and the current component normal to the C line, which is approximately along isobath. Moored and cDrake temperature time series (Fig. 8) agree very well, and the mean differences in temperature are small. Standard deviations of the two time series agree and range from 0.12°C at 2000 dbar to 0.71°C at 420 dbar. The rms differences range from 0.05°C at 2000 dbar to 0.38°C at 420 dbar, and the correlations from $r^2 = 0.83$ to $r^2 = 0.87$ (Fig. 8). Both cDrake and moored time series show similar variability.

At site M2, additional differences between the point moored current and the cDrake mapped current can be expected to arise because the crenulated continental slope topography introduces short alongshore spatial scales in both direction and strength of the current. Moored and cDrake time-varying alongshore (normal component) currents (Fig. 8) are well correlated ($r^2 \geq 0.68$) at 420 and 930 dbar, and moderately correlated ($r^2 = 0.41$) at 2000 dbar. The reduced correlations at deep levels are readily understood: the deeper currents are most affected by the reference barotropic component, which is directly attributable to current meter measurements separated by 16 km across slope; these deep currents are most strongly influenced by the small-scale structure induced by the bottom topography. Moored–cDrake rms differences are approximately the same size as the standard deviations of either source.

M4 was located near the center of the LDA, only 5 km away from CPIES site E02. At this location, mean deep currents flowed west-northwest in a cyclonic barotropic circulation within the Yaghan Basin (Chereskin et al. 2009), and the mean baroclinic shear relative to the bottom was weakly to the east-northeast. At site M4, moored and cDrake time-varying temperatures and currents (Fig. 9) are well correlated ($r^2 \geq 0.68$ for currents, $r^2 \geq 0.85$ for temperatures). The current records of both sources have standard deviations of 7–19 $\mathrm{cm\,s^{-1}}$ and near-isotropic standard deviation ellipses. The rms velocity component (u or v) differences are 11, 8, and 4.5 $\mathrm{cm\,s^{-1}}$, at 520, 1020, and 2540 dbar, respectively (Table 4). The predicted mapping errors for daily

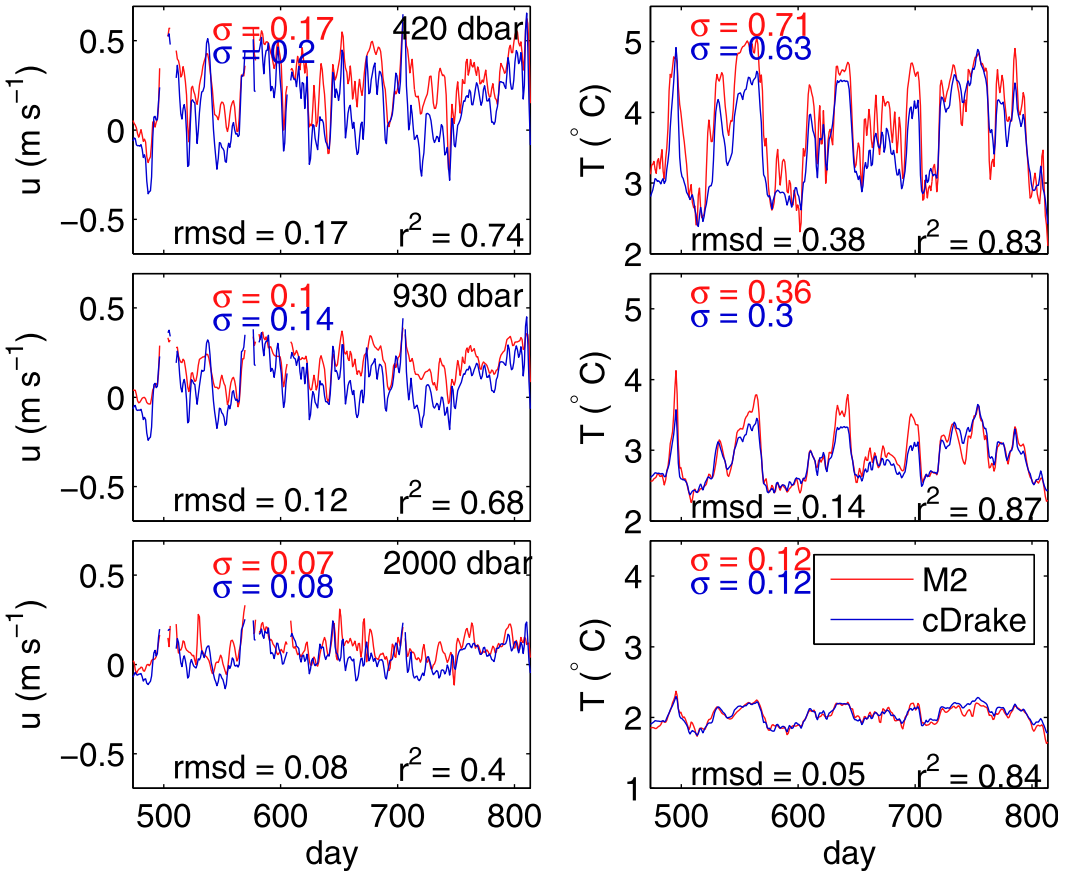

FIG. 8. Daily line-normal (see text) currents and temperature from M2 mooring (red) and cDrake interpolated to mooring $p(t)$ (blue), nominally at (top to bottom) 420, 930, and 2000 dbar. Squared correlation coefficients (r^2), rmsd, and standard deviations of each record (indicated by color) are given in each panel. Velocities from days with >250 dbar mooring drawdown are excluded (see section 2).

current components (Table 3) agree well with these differences as a function of depth.

The 1-yr mean currents at M4 (Table 4; Fig. 10) have similar magnitudes. Their mean directions differ as follows. The cDrake mean currents are directed 21° ± 21°, 18° ± 12°, and 19° ± 6° clockwise of M4 moored mean currents at 520, 1020, and 2540, respectively. (Error brackets for angles are derived from the standard errors of the 1-yr mean current components; see above.) The angle differences at site M4 are mostly due to the reference barotropic-mean currents, which are directly measured by current meters (at 2540 dbar on M4, and near-bottom at nearby site E02 for cDrake). Local topographic steering may play a role in the observed angle differences. In addition, the direction of the angle difference is what would be expected if the near-bottom cDrake currents had been measured within the bottom Ekman layer, and thus rotated clockwise relative to the interior geostrophic current; however, as discussed in section 3d, we expect influence from the bottom boundary layer only 3% of the time. In the following subsection, we will show that mean altimeter surface velocity direction agrees better with the cDrake mapped product than with M4 500-m mean currents.

b. *Comparison with MADT surface currents*

The mean cDrake surface currents compare well with satellite-derived MADT mean surface currents (Figs. 11a,b). Outside of one limited area, surface current vectors agree in size and direction. At mooring site M4, altimeter surface currents are slightly to the right of cDrake surface currents (and even farther to the right of the M4 moored 500-m currents). Both cDrake and MADT capture the Subantarctic Front (SAF) jet and the cyclonic circulation in the northeastern part of the array, with approximately the same locations and magnitudes, over both averaging periods. Where speeds are small, angle uncertainties are larger; note that standard errors of the mean on cDrake mapped mean surface currents are 1–2 cm s^{-1}.

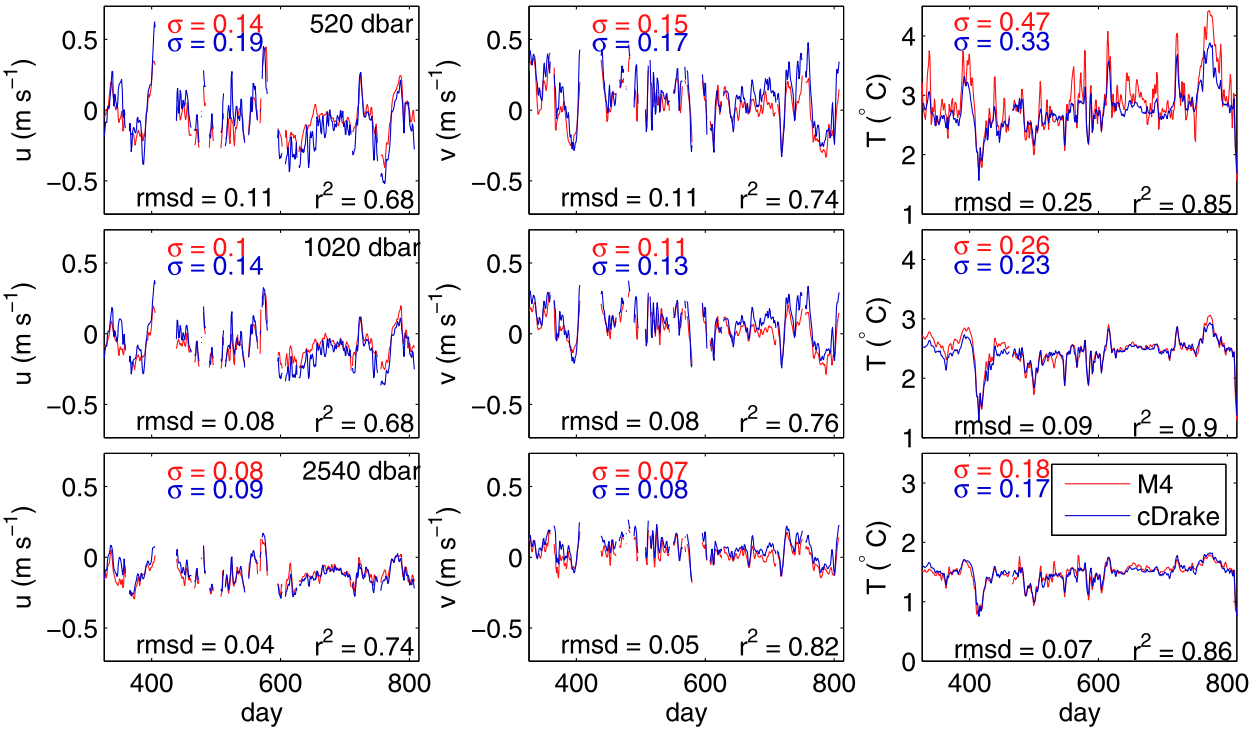

FIG. 9. Daily zonal and meridional currents and temperature from M4 mooring (red) and cDrake interpolated to mooring $p(t)$ (blue), nominally at (top to bottom) 520, 930, and 2540 dbar. Squared correlation coefficients (r^2), rmsd, and standard deviations of each record (indicated by color) are given in each panel. Velocities from days with >250 dbar mooring drawdown are excluded (see section 2).

In an approximately 100 km × 80 km area in the south-central/southwestern part of the LDA, just downstream of the Shackleton Fracture Zone, differences in direction of over 90° are observed, despite the strong currents. These angle differences, which are found in the barotropic reference component in cDrake (Fig. 11c), are supported by deep current measurements from multiple sites, are not an artifact of the mapping, and are present, although reduced in extent, in the 4-yr mean as well as the 1-yr mean. The signs of the differences vary over approximately 50 km and are consistent only at some points with the sign of the rotation associated with bottom boundary layer effects (see section 3d). This suggests the existence of localized features whose space and time scales are too short to be well resolved by the MADT and the associated CNES-CLS09 mean field.

c. *Comparison with LADCP currents*

To compare the directly measured LADCP velocity profiles with the GEM-derived depth profiles, we interpolated cDrake mapped velocity to the positions and times of the 48 selected LADCP casts (section 2). LADCP profiles were boxcar averaged to 100-m vertical bins centered between 100 and 3600 m (the number of available LADCP profiles drops off sharply below this level); cDrake profiles were linearly interpolated to this 100-m grid. We then rotated both cDrake and LADCP velocities, on a cast-by-cast basis, into a local frontal coordinate system based on the angle of the cDrake baroclinic current at each cast, producing frontal-coordinates (fc) profiles $\mathbf{u}_{L,\mathrm{fc}}(z)$ from the LADCP and $\mathbf{u}_{C,\mathrm{fc}}(z)$ from cDrake.

The 48 frontal-coordinates difference profiles (Fig. 12, plotted by cruise to make individual profiles visible), show both high- and low-wavenumber structure. Because the LADCP measures instantaneous total velocity, LADCP profiles contain significant energy due to ageostrophic and small-scale (spatial or temporal) processes, including internal waves, not represented by the cDrake GEM and 3-day low-pass-filtered, objectively mapped fields. To estimate the size of the expected

TABLE 4. Comparison of moored and cDrake velocities (cm s^{-1}) at M4 and time-varying moored pressures. Means and standard deviations of moored and cDrake velocity components, and velocity component mean and rmsd (cm s^{-1}).

Nominal p (dbar)	Moored				cDrake				Moored − cDrake			
	$\langle u\rangle$	$\langle v\rangle$	σ_u	σ_v	$\langle u\rangle$	$\langle v\rangle$	σ_u	σ_v	$\langle u\rangle$	$\langle v\rangle$	rmsd$_u$	rmsd$_v$
520	−5	3	14	15	−7	9	19	18	2	−6	11	11
930	−8	3	10	11	−9	8	14	13	1	−5	8	8
2540	−12	2	8	7	−11	7	9	8	−1	−4	4	5

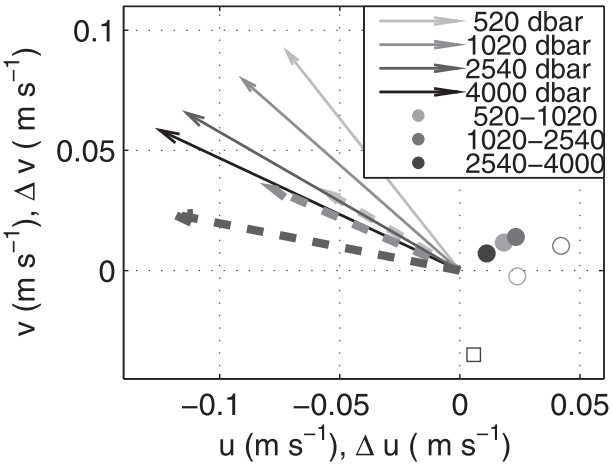

FIG. 10. Mean current vectors from cDrake mapping (solid) and M4 mooring (dashed), and mean vector velocity difference between instrument levels from cDrake mapping (filled circles) and M4 mooring (open circles; square is mean velocity difference between M4 2500-m instrument and cDrake bottom map).

sources of differences between cDrake and LADCP velocity profiles, we divide them into two categories: high-frequency variance, presumably dominated by internal waves and inertial oscillations, and low-frequency submesoscale variance (with spatial scales too short to be captured by the cDrake objective maps). For the first category, we use the standard deviation of the 3-day high-pass-filtered M4 moored velocity component time series, giving 7, 6, and 5 cm s^{-1} at 500, 1000, and 2500 m, respectively. Standard deviations of the 3-day high-pass-filtered near-bottom velocity component records from the nearby E02 CPIES give 6 cm s^{-1} near the bottom, and we assume that the level of high-frequency energy at 500 m is representative of that at 100 m. The 6 cm s^{-1} high-pass-filtered near-bottom variance at E02 is also consistent with the 5 cm s^{-1} rms difference between LADCP bottom and cDrake hourly near-bottom current components. For the lower-frequency contribution we use the rms differences between cDrake and M4 3-day low-pass-filtered velocity component time series, obtaining 11, 8, and 5 cm s^{-1} at 500, 1000, and 2500 m, respectively. We again use the 500-m value for 100 m, and the 2500-m value to represent submesoscale variance at the bottom. Standard deviation intervals resulting from combining variances due to these two sources are shown as thick gray dashed lines in Fig. 12; they envelop approximately two-thirds of the difference profiles, as would be consistent with a normal distribution.

Cruise-mean profiles (Fig. 12, right column) agree reasonably well despite the sampling differences between LADCP and CPIES. The mean difference profiles (Fig. 12, thick black lines) indicate that, as expected

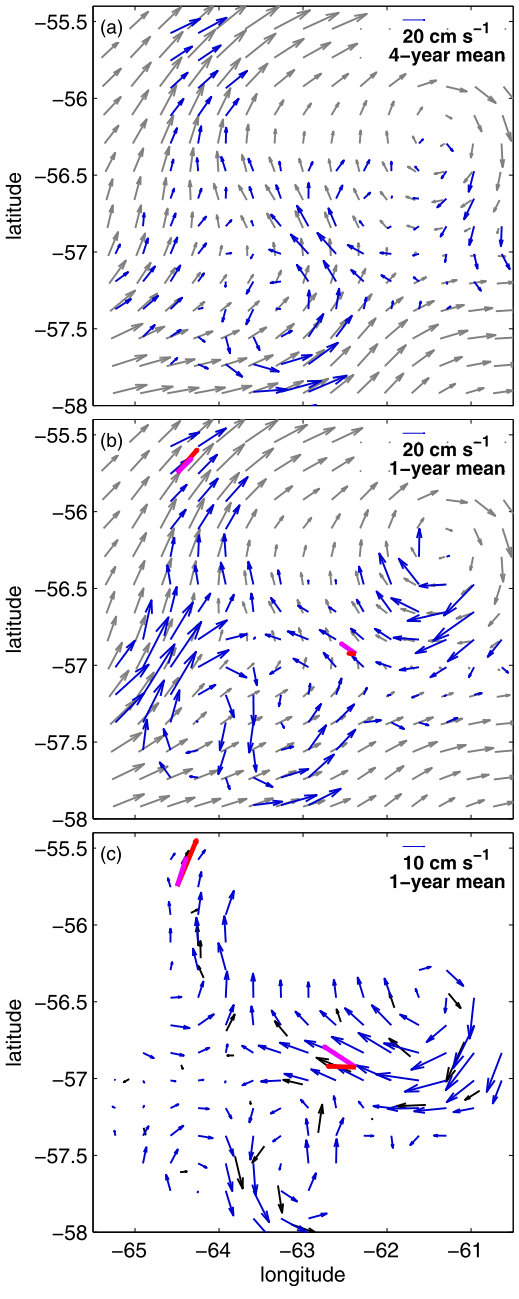

FIG. 11. (a) The 4-yr mean surface currents from cDrake (blue) and MADT (gray). (b) Means over the second M4 deployment period (10 Apr 2008–26 Mar 2009) of MADT (gray) and cDrake (blue) surface currents, with top-mooring-level moored (thick red) and cDrake (thick purple) currents at M2 (420 dbar) and M4 (520 dbar). (c) Means over the second M4 deployment period of cDrake mapped (blue) and measured (black) bottom currents, with bottom-mooring-level moored (thick red) and cDrake (thick purple) currents at M2 (2000 dbar) and M4 (2540 dbar). At the mooring sites, pressure-varying moored and cDrake currents were used. Standard errors of the mean on the cDrake currents are 1–2 cm s^{-1}. The cDrake mapped currents were subsampled from a 10-km grid to a 20-km grid for this plot, and are only shown within the good mapping region (Fig. 1).

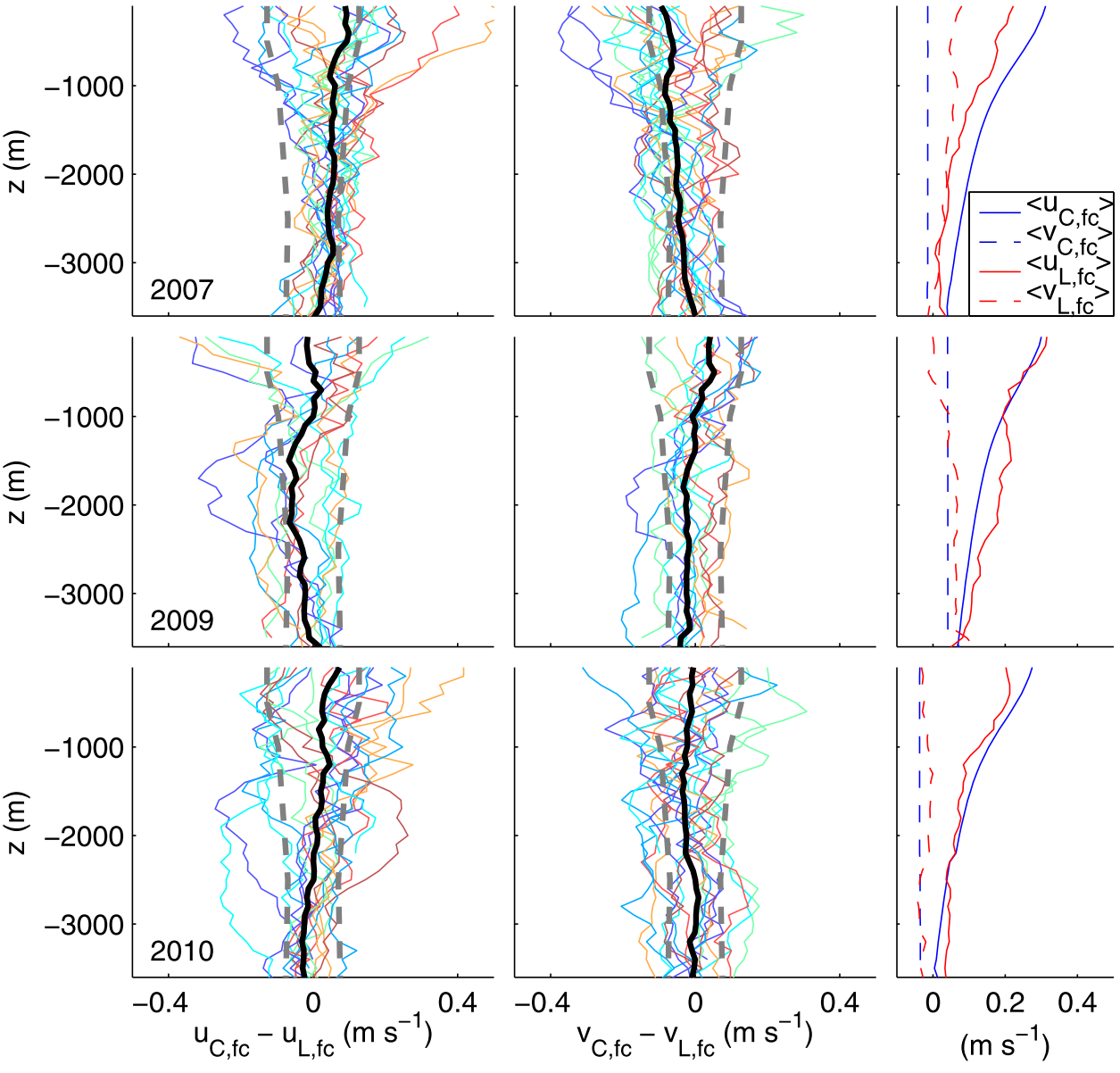

FIG. 12. Frontal-coordinates velocity difference profiles (left) $u_{C,\mathrm{fc}} - u_{L,\mathrm{fc}}$ and (middle) $v_{C,\mathrm{fc}} - v_{L,\mathrm{fc}}$: individual difference profiles (color), mean difference profiles (black), and predicted difference standard deviation intervals (gray dashed lines) for three cruises. (right) Frontal-coordinates cruise-mean velocity profiles from cDrake (blue) and LADCP (red).

for profiles with random angle differences, on average the LADCP alongfront velocity is smaller than the cDrake alongfront velocity, while the LADCP cross-front velocity can be either positive or negative. The relatively small cross-front component of the LADCP mean fc profiles (up to $5\,\mathrm{cm\,s^{-1}}$, as compared to up to $20\,\mathrm{cm\,s^{-1}}$ alongfront) indicates that the LADCP currents are not consistently biased to one side of the cDrake currents at any depth. The frontal-coordinates cruise-mean profiles from the two sources have similarly small barotropic reference components.

7. Summary

We have described a procedure for estimating barotropic and baroclinic geostrophic streamfunction, and its derivatives up to relative vorticity gradients, by objective mapping of time series from an array of CPIES, using spatial scales and noise levels derived from the observations. We extend previous work (Donohue et al. 2010; Meinen et al. 2003; Tracey et al. 1997, 2006; Watts et al. 2001a; and others; see section 1) by mapping directly from bottom p, u, v or from GEM-derived Φ time

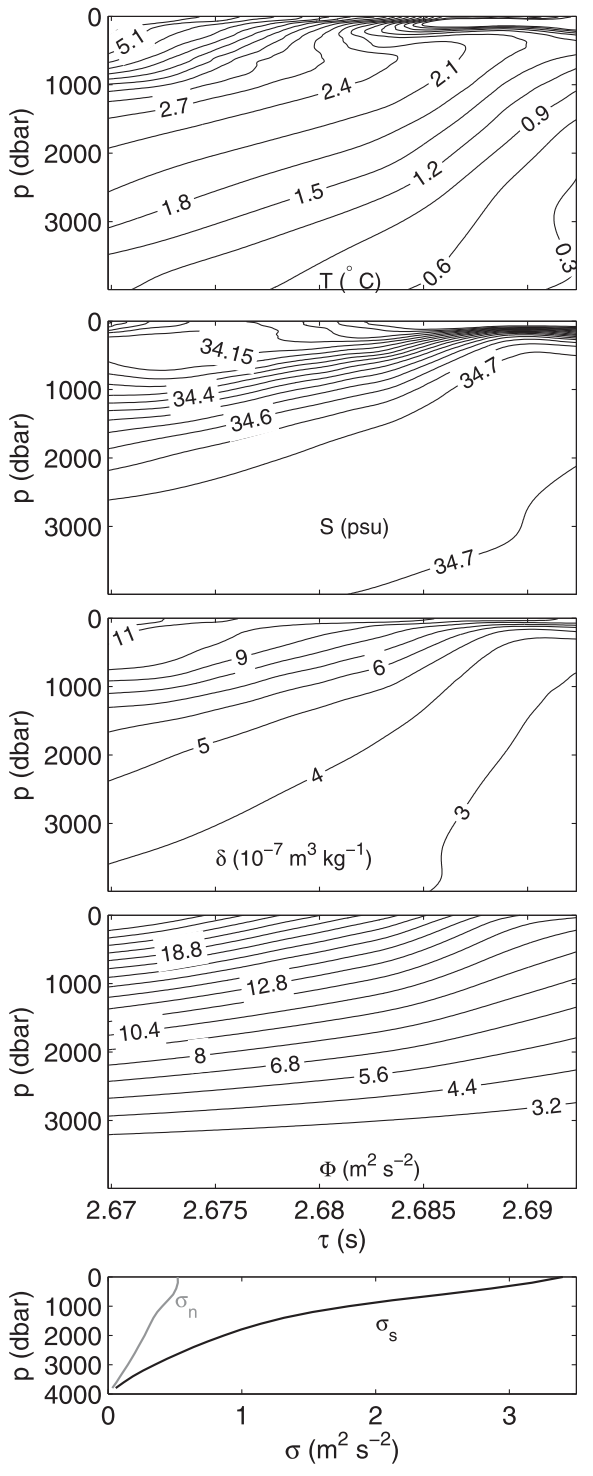

FIG. 13. GEMs for indicated quantities as functions of pressure and τ_{index}, the round-trip acoustic travel time from 0 to 2000 dbar: (top to bottom) T, S, δ, and Φ relative to 4000 dbar. (bottom) Vertical profiles of the standard deviations of the Φ GEM (σ_s, black line) and the Φ anomaly from the GEM (σ_n, gray line, see section 3c).

series to second and third derivatives of streamfunction, thus obtaining improved error estimates relative to methods involving finite differencing, as confirmed by both simulations and comparisons with independent datasets. We have discussed the selection of objective mapping parameters based on the CPIES time series and investigated sensitivity to those parameters. We have also detailed the dimensionalization of mapping errors using spatial variances. Dimensional velocity errors within the good mapping region surrounding the cDrake LDA (Fig. 1) increase from 0.04 m s^{-1} (at 4000 dbar) to 0.11 m s^{-1} at 400 dbar (Table 3) to about 20% larger at the surface, and are thus about 20% of typical eddy speeds at these levels (about 0.2, 0.6, and 0.65 m s^{-1}, respectively). Errors on vorticity and vorticity gradients (Table 3) also decrease with depth, ranging from 3×10^{-6} to 9×10^{-6} s^{-1} (for vorticity; compare with vorticity magnitudes of 1.3×10^{-5} to 4×10^{-5} s^{-1}) and 2×10^{-10} to 4×10^{-10} m^{-1} s^{-1} (for vorticity gradients; compare with gradient magnitudes of 5×10^{-10} to 10×10 m^{-1} s^{-1}).

Objective mapping of a simulated field shows the following: 1) In the center of the array, with noise-to-signal ratio n comparable to those calculated for the cDrake streamfunction and velocity, mapping from either single (streamfunction ψ) or multivariable (ψ, u, v) input can reproduce daily values of variables up to second derivatives of ψ to within the error estimates described in section 3e. 2) The mapping error estimates accurately reflect the deviations of the mapped fields from the analytic values. Time series smoothed with a 7-day Butterworth filter capture both the signs and relative magnitudes of the analytic terms of both the zonal momentum balance and the vorticity balance (including terms up to third derivatives of ψ). The simulations also show that our mapping error estimates are accurate, giving us confidence that with appropriate smoothing or averaging we can calculate momentum and vorticity balance quantities and their uncertainties from observations. Unlike the simulated data, the cDrake measurements do not have a clear dominant period; the degree of smoothing for a given calculation should be chosen to balance the competing desires for time resolution and reduced noise in higher-order terms.

Comparisons between cDrake-mapped and LADCP-measured velocity profiles collected on the cDrake cruises confirm that the cDrake mapping and GEM method accurately reproduces the dominant vertical structure of the mesoscale geostrophic current. Additionally, the cDrake-mapped surface currents and satellite-altimeter-derived surface currents agree well except in a small region where short space and time scales may not be well resolved by the altimeter, distorting its estimated mean

dynamic topography. Mapped cDrake temperatures, currents, and current shear compare very well with those measured at moorings M4 (in the LDA) and M2 (just north of the LDA). The high correlations and small offsets confirm the cDrake method described here for computing velocities. Both baroclinic and barotropic variability are reproduced.

This work has focused on methods for producing maps of the mesoscale geostrophic flow field in Drake Passage from CPIES measurements. The simulations and the comparisons with independent data give us confidence that the method described here can be used to compute higher-order derivatives of daily geostrophic streamfunction in the interior of a two-dimensional array of CPIES like the cDrake LDA, with accurate uncertainty estimates. Additional investigations using these mapped fields to elucidate various mesoscale processes occurring in Drake Passage are ongoing and include examination of the role of eddies in the momentum and vorticity balances and in the transport of heat, buoyancy, and potential vorticity.

Acknowledgments. We are particularly grateful to Kathleen Donohue for coleading the cDrake project and for providing extensive advice on numerous issues in this manuscript. The optimal interpolation codes developed for this work build on earlier codes developed by Xiaoshu Qian and Christopher Meinen. The LADCP data were processed using publicly available software, and we are grateful to the software developers and maintainers: E. Firing, M. Visbeck, A. Thurnherr, and G. Krahmann. XCTD data were provided by J. Sprintall. The National Science Foundation Office of Polar Programs supported this work under NSF Grants ANT-0636493 (SIO cDrake) and ANT-0635437 (URI cDrake). Y. Firing was supported by NASA Earth Systems Science Fellowship NNX09AN87H. We thank G. Chaplin, S. Escher, D. Holloway, E. Sousa, the captains and crew of the RVIB *Nathaniel B. Palmer*, and Raytheon Polar Services for technical and logistical support during the cDrake cruises.

APPENDIX A

cDrake GEM

Nearly 600 historical hydrogaphic casts (CTDs and Argo floats, section 2) were used to compute temperature (T), salinity (S), and specific volume anomaly (δ) gravest empirical mode lookup tables (GEMs) as functions of τ_{index}, as described by Meinen and Watts (2000) and Donohue et al. (2010). For the cDrake GEMs, τ_{index} is the integrated round-trip travel time between the surface and 2000 dbar; this lower bound was chosen so that Argo float profiles could be incorporated into the GEMs. The specific volume anomaly (δ) profiles were computed from the CTD temperature and salinity profiles using the SEAWATER toolbox for MATLAB (Morgan 1994). GEM curves were computed by fitting smoothing splines to the relationships of T, S, and δ with τ_{index} at a suite of pressure levels ranging from 0 to 3800 dbar. Levels (Firing 2012) are spaced at increments of 10 dbar in the upper 310 dbar, increasing with depth to up to 400-dbar spacing (as the number of hydrocasts changes with depth, use of closely spaced pressure levels for fitting can lead to overlapping spline curves). The GEMs were extended below 3800 dbar, where available data are sparse, by offsetting the curves at 3800 dbar to agree with the mean at each deeper level. The smoothing parameter varied with depth; smoothing increased with depth as the number of casts declined. Following Sun and Watts (2001), we estimated the a priori error profile and compared it with the GEM rms error profile to confirm that the appropriate amount of smoothing was performed. The GEM curves were then vertically interpolated to 10-dbar pressure resolution using cubic splines. A GEM for Φ relative to 4000 dbar was computed by integrating δ_{GEM} from a reference pressure, $p_r = 4000$ dbar (see section 3d below), to each pressure level using

$$\Phi_{\text{GEM}}(p,\tau) = \int_{p_r}^{p} \delta_{\text{GEM}}(p',\tau)\, dp'. \qquad \text{(A1)}$$

The T, S, δ, and Φ GEMs are shown in Fig. 13. The T, S, and δ fields exhibit characteristics similar to the GEMs calculated by Sun and Watts (2001) for the Drake Passage as functions of geopotential height rather than travel time.

The $\tau_{\text{index}}(t)$ at each CPIES site is used to look up $\Phi(p, \tau)$ in the GEM by linear interpolation, obtaining a time series of $\Phi(p, t)$. Using the array of Φ records, we then objectively map (section 3) $\Phi(x, y, p, t)$ to baroclinic streamfunction (relative to 4000 dbar), and its derivatives. Except where otherwise specified, $\Phi(p, t)$ and subsequent derivative fields were examined at 200-dbar intervals from 0 to 4000 dbar. Estimates of uncertainties (section 3e) are smaller (by factors ranging from 2 for velocity up to an order of magnitude for third derivatives of streamfunction) when τ is interpolated to Φ and objectively mapped to the baroclinic streamfunction and its derivatives than when τ is mapped and then converted to Φ and its derivatives using finite difference estimates of $\partial\Phi/\partial\tau$, $\partial^2\Phi/\partial\tau^2$, and $\partial^3\Phi/\partial\tau^3$. The comparisons discussed in this paper (sections 4 and 6) verified that the small mapping error estimates are accurate. We detail the Φ GEM contribution to error in section 3c.

APPENDIX B

Covariances for Objective Mapping

Following Qian and Watts (1992) and Gille (2003), we derive the relationships necessary to objectively map to second and higher derivatives of the streamfunction $\psi = p/\rho_0$ or $\psi = \Phi$. We will map to

$$u_{\text{map}} = -\frac{\partial \psi}{\partial y}, \tag{B1}$$

$$v_{\text{map}} = \frac{\partial \psi}{\partial x}, \tag{B2}$$

$$v_{\text{mapx}} = \psi_{xx}, \tag{B3}$$

$$v_{\text{mapy}} = -u_{\text{mapx}} = \psi_{xy}, \tag{B4}$$

$$u_{\text{mapy}} = -\psi_{yy}, \tag{B5}$$

$$\zeta_{\text{map}} = v_{\text{mapx}} - u_{\text{mapy}} = \psi_{xx} + \psi_{yy}, \tag{B6}$$

$$\zeta_{\text{mapx}} = \nabla^2 v = \psi_{xxx} + \psi_{xyy}, \tag{B7}$$

$$\zeta_{\text{mapy}} = -\nabla^2 u = \psi_{xxy} + \psi_{yyy}, \tag{B8}$$

where $(u_{\text{map}}, v_{\text{map}}) = (fu, fv)$. We can then convert from mapping variables to the real geostrophic velocity and other variables by

$$u = u_{\text{map}}/f, \tag{B9}$$

$$v = v_{\text{map}}/f, \tag{B10}$$

$$u_x = u_{\text{mapx}}/f, \tag{B11}$$

$$u_y = (u_{\text{mapy}} - \beta u)/f, \tag{B12}$$

$$v_x = v_{\text{mapx}}/f, \tag{B13}$$

$$v_y = (v_{\text{mapy}} - \beta v)/f, \tag{B14}$$

$$\zeta = (\zeta_{\text{map}} + \beta u)/f, \tag{B15}$$

$$\zeta_x = (\zeta_{\text{mapx}} + \beta u_x)/f, \quad \text{and} \tag{B16}$$

$$\zeta_y = (\zeta_{\text{mapy}} - \beta\zeta + \beta u_y + \beta_y u)/f. \tag{B17}$$

In the rest of this section, the subscript map will be dropped but all variables will be mapping variables. Some of the relations in appendix A in Qian and Watts (1992) are repeated below for reference.

a. Covariance of ψ

We assume, after verifying for the LDA variability that observed meridional, zonal, and diagonal correlations are not statistically different, an isotropic Gaussian covariance for ψ as shown:

$$F_{\psi\psi} = \langle \psi(x_1, y_1)\psi(x_2, y_2)\rangle = F = V_\psi e^{-\lambda\gamma^2}, \quad \text{and} \tag{B18}$$

$$F' = \frac{dF}{d\gamma} = -2\lambda\gamma F, \tag{B19}$$

where $F = F(\gamma)$ is a function of the separation γ; $\lambda = 1/L^2$, where L is the correlation length scale; and V_ψ is the amplitude of $F_{\psi\psi}$ at zero separation. In the objective mapping implementation $V_\psi = 1 - E \simeq 1/(1 + E)$, where E is the noise-to-signal variance ratio.

b. Separations

To derive the covariances between other variables given above, we will need to take derivatives with respect to the x and y positions, for which the following will be useful [in the following, the $\cos\alpha_x$, $\cos\alpha_y$ in appendix A of Qian and Watts (1992) are replaced by r, s]:

$$\gamma = \sqrt{(x_1 - x_2)^2 + (y_1 - y_2)^2}, \tag{B20}$$

$$x_2 - x_1 = \gamma r, \quad r = \cos\theta, \tag{B21}$$

$$y_2 - y_1 = \gamma s, \quad s = \sin\theta, \quad \text{and} \tag{B22}$$

$$r^2 + s^2 = 1, \tag{B23}$$

where θ is the angle between (x_1, y_1) and (x_2, y_2), and

$$-\frac{\partial\gamma}{\partial x_1} = \frac{\partial\gamma}{\partial x_2} = r, \tag{B24}$$

$$-\frac{\partial\gamma}{\partial y_1} = \frac{\partial\gamma}{\partial y_2} = s. \tag{B25}$$

$$-\frac{\partial r}{\partial x_1} = \frac{\partial r}{\partial x_2} = \frac{1}{\gamma}(1 - r^2) = \frac{1}{\gamma}s^2, \tag{B26}$$

$$-\frac{\partial s}{\partial y_1} = \frac{\partial s}{\partial y_2} = \frac{1}{\gamma}(1 - s^2) = \frac{1}{\gamma}r^2, \tag{B27}$$

$$\frac{\partial r}{\partial y_1} = -\frac{\partial r}{\partial y_2} = \frac{1}{\gamma}rs, \quad \text{and} \tag{B28}$$

$$\frac{\partial s}{\partial x_1} = -\frac{\partial s}{\partial x_2} = \frac{1}{\gamma}rs. \tag{B29}$$

c. Cross covariances $F_{\psi *}$

We calculate the cross covariances following Gille (2003) using

$$F_{\psi u} = -F_{\psi\psi_y} = -\frac{\partial}{\partial y_2}F = 2\lambda\gamma s F, \tag{B30}$$

$$F_{\psi v} = F_{\psi\psi_x} = \frac{\partial}{\partial x_2}F = -2\lambda\gamma r F, \tag{B31}$$

$$F_{\psi v_x} = F_{\psi\psi_{xx}} = \frac{\partial}{\partial x_2}F_{\psi\psi_x} = -2\lambda(1-2\lambda\gamma^2 r^2)F, \tag{B32}$$

$$F_{\psi v_y} = -F_{\psi u_x} = F_{\psi\psi_{xy}} = \frac{\partial}{\partial x_2}F_{\psi\psi_y} = 4\lambda^2\gamma^2 rs F, \tag{B33}$$

$$-F_{\psi u_y} = F_{\psi\psi_{yy}} = \frac{\partial}{\partial y_2}F_{\psi\psi_y} = -2\lambda(1-2\lambda\gamma^2 s^2)F, \tag{B34}$$

$$F_{\psi\zeta} = F_{\psi\psi_{xx}} + F_{\psi\psi_{yy}} = 4\lambda(\lambda\gamma^2 - 1)F, \tag{B35}$$

$$F_{\psi\zeta_x} = F_{\psi\nabla^2 v} = \frac{\partial}{\partial x_2}F_{\psi\zeta} = 8\lambda^2\gamma r(2-\lambda\gamma^2)F, \tag{B36}$$

$$F_{\psi\zeta_y} = -F_{\psi\nabla^2 u} = \frac{\partial}{\partial y_2}F_{\psi\zeta} = 8\lambda^2\gamma s(2-\lambda\gamma^2)F, \tag{B37}$$

as $(\partial/\partial x_1) = -(\partial/\partial x_2)$, and similarly for y_1, y_2, $F_{\psi\psi_x} = -F_{\psi_x\psi}$, $F_{\psi\psi_{xx}} = F_{\psi_{xx}\psi}$, $F_{\psi\psi_{xxx}} = -F_{\psi_{xxx}\psi}$, etc.

d. Cross covariances $F_{u *}$, $F_{v *}$

At the seafloor, we measure u, v as well as the streamfunction and can map from the three variables ψ, u, v to each desired variable using

$$F_{u\psi} = -F_{\psi u} = -2\lambda\gamma s F, \tag{B38}$$

$$F_{v\psi} = -F_{\psi v} = 2\lambda\gamma r F, \tag{B39}$$

$$F_{uu} = -\frac{\partial}{\partial y_1}F_{\psi u} = 2\lambda(1-2\lambda\gamma^2 s^2)F, \tag{B40}$$

$$F_{uv} = F_{vu} = \frac{\partial}{\partial x_1}F_{\psi u} = 4\lambda^2\gamma^2 rs F, \tag{B41}$$

$$F_{vv} = \frac{\partial}{\partial x_1}F_{\psi v} = 2\lambda(1-2\lambda\gamma^2 r^2)F, \tag{B42}$$

$$F_{uv_x} = -\frac{\partial}{\partial y_1}F_{\psi v_x} = 4\lambda^2\gamma s(1-2\lambda\gamma^2 r^2)F, \tag{B43}$$

$$F_{uv_y} = -F_{uu_x} = -\frac{\partial}{\partial y_1}F_{\psi v_y} = 4\lambda^2\gamma r(1-2\lambda\gamma^2 s^2)F, \tag{B44}$$

$$F_{uu_y} = -\frac{\partial}{\partial y_1}F_{\psi u_y} = -4\lambda^2\gamma s(3-2\lambda\gamma^2 s^2)F, \tag{B45}$$

$$F_{u\zeta} = -\frac{\partial}{\partial y_1}F_{\psi\zeta} = 8\lambda^2\gamma s(2-\lambda\gamma^2)F, \tag{B46}$$

$$F_{vv_x} = \frac{\partial}{\partial x_1}F_{\psi v_x} = -4\lambda^2\gamma r(3-2\lambda\gamma^2 r^2)F, \tag{B47}$$

$$F_{vv_y} = -F_{vu_x} = \frac{\partial}{\partial x_1}F_{\psi v_y} = -4\lambda^2\gamma s(1-2\lambda\gamma^2 r^2)F, \tag{B48}$$

$$F_{vu_y} = \frac{\partial}{\partial x_1}F_{\psi u_y} = 4\lambda^2\gamma r(1-2\lambda\gamma^2 s^2)F, \tag{B49}$$

$$F_{v\zeta} = \frac{\partial}{\partial x_1}F_{\psi\zeta} = -8\lambda^2\gamma r(2-\lambda\gamma^2)F, \tag{B50}$$

$$F_{u\zeta_x} = F_{u\nabla^2 v} = -\frac{\partial}{\partial y_1}F_{\psi\zeta_x} = -16\lambda^3\gamma^2 rs(3-\lambda\gamma^2)F, \tag{B51}$$

$$F_{u\zeta_y} = -F_{u\nabla^2 u} = -\frac{\partial}{\partial y_1}F_{\psi\zeta_y} = 8\lambda^2(2-6\lambda\gamma^2 s^2-\lambda\gamma^2+2\lambda^2\gamma^4 s^2)F, \tag{B52}$$

$$F_{v\zeta_x} = F_{v\nabla^2 v} = \frac{\partial}{\partial x_1}F_{\psi\zeta_x} = -8\lambda^2(2-6\lambda\gamma^2 r^2-\lambda\gamma^2+2\lambda^2\gamma^4 r^2)F, \quad \text{and} \tag{B53}$$

$$F_{v\zeta_y} = -F_{v\nabla^2 u} = \frac{\partial}{\partial x_1}F_{\psi\zeta_y} = 16\lambda^3\gamma^2 rs(3-\lambda\gamma^2)F. \tag{B54}$$

As explained above, $F_{uu_x} = -F_{u_x u}, F_{uu_{xx}} = F_{u_{xx}u}$, etc.

e. Normalization factors: $F_{**}(\gamma = 0)$

To compute the mapping skill, we require the amplitudes of the autocovariances at zero separation. We already have F_{uu} and F_{vv}. With $\gamma = 0$ we have

$$F_{u_x u_x} = \frac{\partial}{\partial x_1}F_{uu_x} = 4\lambda^2 F(0), \tag{B55}$$

$$F_{u_y u_y} = \frac{\partial}{\partial y_1}F_{uu_y} = 12\lambda^2 F(0), \tag{B56}$$

$$F_{v_x v_x} = \frac{\partial}{\partial x_1}F_{vv_x} = 12\lambda^2 F(0), \tag{B57}$$

$$F_{v_y v_y} = \frac{\partial}{\partial y_1}F_{vv_y} = 4\lambda^2 F(0), \tag{B58}$$

$$F_{\zeta\zeta} = \frac{\partial}{\partial x_1} F_{v\zeta} - \frac{\partial}{\partial y_1} F_{u_\zeta} = 32\lambda^2 F(0), \qquad \text{(B59)}$$

$$F_{\zeta_x\zeta_x} = \frac{\partial^2}{\partial x_1 x_2} F_{\zeta\zeta} = 192\lambda^3 F(0), \quad \text{and} \qquad \text{(B60)}$$

$$F_{\zeta_y\zeta_y} = \frac{\partial^2}{\partial y_1 y_2} F_{\zeta\zeta} = 192\lambda^3 F(0). \qquad \text{(B61)}$$

REFERENCES

Baker-Yeboah, S., 2008: Sea surface height variability and the structure of eddies in the South Atlantic cape basin. Ph.D. thesis, University of Rhode Island, 336 pp. [Available online at http://search.proquest.com//docview/304507313.]

——, D. R. Watts, and D. A. Byrne, 2009: Measurements of sea surface height variability in the eastern South Atlantic from pressure sensor–equipped inverted echo sounders: Baroclinic and barotropic components. *J. Atmos. Oceanic Technol.,* **26,** 2593–2609.

Behnisch, M., A. Macrander, O. Boebel, J.-O. Wolff, and J. Schröter, 2013: Barotropic and deep-referenced baroclinic SSH variability derived from pressure inverted echo sounders (PIES) south of Africa. *J. Geophys. Res. Oceans,* **118,** 3046–3058, doi:10.1002/jgrc.20195.

Bretherton, F. P., R. E. Davis, and C. B. Fandry, 1976: A technique for objective analysis and design of oceanographic experiments applied to MODE-73. *Deep-Sea Res.,* **23,** 559–582.

Chereskin, T. K., K. A. Donohue, D. R. Watts, K. L. Tracey, Y. L. Firing, and A. L. Cutting, 2009: Strong bottom currents and cyclogenesis in Drake Passage. *Geophys. Res. Lett.,* **36,** L23602, doi:10.1029/2009gl040940.

——, ——, and ——, 2012: cDrake: Dynamics and transport of the Antarctic Circumpolar Current in Drake Passage. *Oceanography,* **25,** 134–135.

Cronin, M., and D. R. Watts, 1996: Eddy–mean flow interaction in the Gulf Stream at 68°W. Part I: Eddy energetics. *J. Phys. Oceanogr.,* **26,** 2107–2131.

Csanady, G. T., 1967: The ''resistance law'' of a turbulent Ekman layer. *J. Atmos. Sci.,* **24,** 467–471.

Cutting, A. L., 2010: Constituents of sea surface height variability in Drake Passage. M.S. thesis, Graduate School of Oceanography, University of Rhode Island, 68 pp. [Available online at http://www.po.gso.uri.edu/dynamics/publications/thesis/Cutting_pothesis.pdf.]

Donohue, K. A., D. R. Watts, K. L. Tracey, A. D. Greene, and M. Kennelly, 2010: Mapping circulation in the Kuroshio Extension with an array of current and pressure recording inverted echo sounders. *J. Atmos. Oceanic Technol.,* **27,** 507–527.

Egbert, G. D., A. F. Bennett, and M. G. G. Foreman, 1994: TOPEX/Poseidon tides estimated using a global inverse model. *J. Geophys. Res.,* **99** (C12), 24 821–24 852, doi:10.1029/94jc01894.

Ferrari, R., C. Provost, A. Renault, N. Sennéchael, N. Barré, Y.-H. Park, and J. H. Lee, 2012: Circulation in Drake Passage revisited using new current time series and satellite altimetry. Part I: The Yaghan Basin. *J. Geophys. Res.,* **117,** C12024, doi:10.1029/2012jc008264.

Firing, Y. L., 2012: Structure and dynamical balance of the Antarctic Circumpolar Current in Drake Passage. Ph.D. thesis, University of California, San Diego, 190 pp. [Available online at http://search.proquest.com/docview/1269794836.]

Gille, S. T., 2003: Float observations of the Southern Ocean. Part I: Estimating mean fields, bottom velocities, and topographic steering. *J. Phys. Oceanogr.,* **33,** 1167–1181.

Howden, S. D., and D. R. Watts, 1999: Jet streaks in the Gulf Stream. *J. Phys. Oceanogr.,* **29,** 1910–1924.

Kennelly, M. A., K. L. Tracey, and D. R. Watts, 2007: Inverted echo sounder data processing manual. Graduate School of Oceanography Tech. Rep. 2007-02, University of Rhode Island, 89 pp. [Available online at http://digitalcommons.uri.edu/physical_oceanography_techrpts/2.]

Meijers, A. J. S., N. L. Bindoff, and S. R. Rintoul, 2011a: Estimating the four-dimensional structure of the Southern Ocean using satellite altimetry. *J. Atmos. Oceanic Technol.,* **28,** 548–568.

——, ——, and ——, 2011b: Frontal movements and property fluxes: Contributions to heat and freshwater trends in the Southern Ocean. *J. Geophys. Res.,* **116,** C08024, doi:10.1029/2010JC006832.

Meinen, C. S., and D. R. Watts, 1998: Calibrating inverted echo sounders equipped with pressure sensors. *J. Atmos. Oceanic Technol.,* **15,** 1339–1345.

——, and ——, 2000: Vertical structure and transport on a transect across the North Atlantic Current near 42°N: Time series and mean. *J. Geophys. Res.,* **105** (C9), 21 869–21 891.

——, and D. S. Luther, 2002: Combining inverted echo sounder and horizontal electric field recorder measurements to obtain absolute velocity profiles. *J. Atmos. Oceanic Technol.,* **19,** 1653–1664.

——, ——, D. R. Watts, A. D. Chave, and K. L. Tracey, 2003: Mean stream coordinates structure of the Subantarctic Front: Temperature, salinity, and absolute velocity. *J. Geophys. Res. Oceans,* **108,** 3263, doi:10.1029/2002jc001545.

Morgan, P. P., 1994: SEAWATER: A library of MATLAB computational routines for the properties of sea water: Version 1.2. CSIRO Marine Laboratories Rep. 222, 29 pp.

Munk, W. H., and D. E. Cartwright, 1966: Tidal spectroscopy and prediction. *Philos. Trans. Roy. Soc. London,* **A259,** 533–581.

Orsi, A. H., T. Whitworth III, and W. D. Nowlin Jr., 1995: On the meridonal extent and fronts of the Antarctic Circumpolar Current. *Deep-Sea Res. I,* **42,** 641–673.

Qian, X., and D. R. Watts, 1992: The SYNOP experiment: Bottom pressure maps for the central array May 1988 to August 1990. Graduate School of Oceanography Tech. Rep. 92-3, University of Rhode Island, 185 pp.

Sprintall, J., T. K. Chereskin, and C. Sweeney, 2012: High-resolution underway upper ocean and surface atmospheric observations in Drake Passage: Synergystic measurements for climate science. *Oceanography,* **25,** 70–81, doi:10.5670/oceanog.2012.77.

Sun, C., and D. R. Watts, 2001: A circumpolar gravest empirical mode for the Southern Ocean hydrography. *J. Geophys. Res.,* **106** (C2), 2833–2855.

Swart, S., S. Speich, I. J. Ansorge, and J. R. E. Lutjeharms, 2010: An altimetry-based gravest empirical mode south of Africa: 1. Development and validation. *J. Geophys. Res.,* **115,** C03002, doi:10.1029/2009JC005299.

Thurnherr, A. M., 2010: A practical assessment of the errors associated with full-depth LADCP profiles obtained using Teledyne RDI Workhorse acoustic Doppler current profilers. *J. Atmos. Oceanic Technol.,* **27,** 1215–1227.

Tracey, K. L., S. D. Howden, and D. R. Watts, 1997: IES calibration and mapping procedures. *J. Atmos. Oceanic Technol.,* **14,** 1483–1493.

——, D. R. Watts, C. S. Meinen, and D. S. Luther, 2006: Synoptic maps of temperature and velocity within the Subantarctic Front south of Australia. *J. Geophys. Res.,* **111,** C10016, doi:10.1029/2005jc002905.

——, K. A. Donohue, D. R. Watts, and T. Chereskin, 2013: cDrake CPIES data report November 2007 to December 2011. Graduate School of Oceanography Tech. Rep. 2013-01, University of Rhode Island, 80 pp. [Available online at http://digitalcommons.uri.edu/physical_oceanography_techrpts/4.]

Visbeck, M., 2002: Deep velocity profiling using lowered acoustic Doppler current profilers: Bottom track and inverse solutions. *J. Atmos. Oceanic Technol.,* **19,** 794–807.

Watts, D. R., X. Qian, and K. L. Tracey, 2001a: Mapping abyssal current and pressure fields under the meandering Gulf Stream. *J. Atmos. Oceanic Technol.,* **18,** 1052–1067.

——, C. Sun, and S. Rintoul, 2001b: A two-dimensional gravest empirical mode determined from hydrographic observations in the Subantarctic Front. *J. Phys. Oceanogr.,* **31,** 2186–2209.